

MOX-Report No. 84/2026

From Excitability to Multistability: A Detailed Bifurcation Analysis of the Barreto-Cressman-type Neural Models

Kumar, N.; Pagani, S.; Antonietti, F. P.; Singh, S.

MOX, Dipartimento di Matematica
Politecnico di Milano, Via Bonardi 9 - 20133 Milano (Italy)

mox-dmat@polimi.it https://mox.polimi.it

From Excitability to Multistability: A Detailed Bifurcation Analysis of the Barreto-Cressman-type Neural Models

Niteen Kumar[1*], Stefano Pagani[1], Paola F. Antonietti[1], Suneet Singh[2]

[1*]MOX, Dipartimento di Matematica , Politecnico di Milano, Via Bonardi 9, Milano, 20133, , Italy.
[2]Department of Energy Sciences and Engineering, Indian Institute of Technology Bombay, , Mumbai, 400076, Maharashtra, India.

*Corresponding author(s). E-mail(s): niteenkumar@polimi.it;
Contributing authors: stefano.pagani@polimi.it;
paola.antonietti@polimi.it; suneet.singh@iitb.ac.in;

Abstract

Neuronal dynamics operate on multiple time scales, with membrane potential evolving on a fast scale coupled with ionic concentrations varying on a slower scale. Changes in ionic concentrations play a key role in regulating neuronal excitability and spiking activity, leading to bursting behavior under specific conditions. This study provides a bifurcation analysis of the Barreto-Cressman and reduced Barreto–Cressman models, as well as the unified Barreto–Cressman model, to identify the parameter range for the occurrence of bursting activity. With one-parameter bifurcation analysis, we identified critical transition points such as limit points, Hopf points, and limit points of cycles, and the parameter range for stable, oscillatory, and multistable behavior. With two-parameter bifurcation analysis, we identified high-order bifurcation points, including cusp, Bogdanov–Takens, and generalized Hopf points, and delineated regions of different behaviors and transitions between bursting and non-bursting states. The numerical comparison shows that, for low values of bath potassium concentration and pump strength, there is good agreement between the reduced Barreto–Cressman and the Barreto–Cressman models. For higher values of bath potassium concentration, a significant shift in the bifurcation points is observed, resulting in discrepancies in the dynamical behavior of neurons. By adding the $[Cl]^-$ dynamics to the full model, a unified model is developed. The bifurcation

analysis of the unified model contributes to a more comprehensive understanding of bursting behavior in neuronal systems and may have potential implications for seizure modeling, prediction, and control strategies.

Keywords: Neural Dynamics, Bursting, Seizure, Ion Dynamics, Bifurcation Analysis

1 Introduction

Neurons operate on two principal time scales: fast dynamics (membrane action potential and gating variables) vary on the order of milliseconds, while slow dynamics (ion concentrations) vary on the order of seconds [1–5]. The coexistence of multiple time scales in a highly nonlinear system makes the model stiff. Such systems are very sensitive to operating parameters and can show a whole new behavior such as quiescence, spiking, and bursting, under varying parameter conditions. Bursting is referred to as the active phase with self-sustained high-frequency oscillations followed by a return to a resting state (silent phase) [6, 7]. A series of synchronous bursts in a neuronal network, with abrupt onset and offset, is associated with seizure activity [8]. Understanding the mechanisms underlying burst formation and their inhibition is essential to advance effective seizure control strategies.

Hodgkin and Huxley are among the very first to develop a mathematical model of neural electrophysiology [9]. However, this is a simplified phenomenological model, considers only the fast time scale, and treats the slow-scale variables (ion concentrations) as system parameters. Following this, a few simplified models like the Morris-Lecar and FitzHugh–Nagumo were developed from the Hodgkin - Huxley model. Morris-Lecar model is a two-dimensional model consisting of a fast membrane action potential and a slow recovery variable, which can be easily projected onto a 2D phase plane, and geometrical tools like nullcline analysis can be used [10]. With further simplification of the Morris-Lecar model, the FitzHugh-Nagumo model is developed for the same two variables, fast membrane action potential and slow recovery variable, with algebraic coefficients that can be tuned to mimic desired behavior [11]. By incorporating slow ion concentration dynamics into the Hodgkin–Huxley model, Cressman et. al. were among the first to develop a more generalized mathematical model, known as the Barreto-Cressman (BC) model, describing both slow and fast dynamics, capable of capturing both physiological and pathological behavior [2, 3]. A key feature of the BC model is that the ion concentrations are allowed to evolve dynamically. This model involves the following quantities: the membrane action potential (V), the gating variables (responsible for the opening and closing of ion channels), and ion concentration dynamics like Potassium $[K]^+$, Sodium $[Na]^+$, calcium $[Ca]^{2+}$, and chloride $[Cl]^-$. The BC model is parametrized such that a wide range of scenarios from "physiological to pathological" can be simulated just by altering parameter values without making any modification to the governing system of equations. The reversal potential of an ion depends on the ratio of its intracellular and extracellular concentrations. Therefore, changes in ion concentration affect the reversal potential of ions as well. The increase in the concentration of extracellular potassium $[K^+]_o$ and decrease in

intracellular sodium $[Na^+]_i$ lead to an increase in their respective reversal potentials [12–15]; glial cells slowly clear extracellular ions, bringing down the ion concentration to its normal physiological range and restoring the normal spiking behavior [2, 3]. In the case of low $[K^+]$ and $[Na^+]$ concentrations, alternatively, spiking activity can be maintained by an external stimulus current as a control parameter. This detailed description of ionic dynamics given by the BC model makes it possible to study bursting activity [2, 16]. To this goal, building on the work of Cressman et. al. [2], Wei et. al. unified the dynamics of multiple ionic species—potassium, sodium, chloride, and oxygen—with the Hodgkin–Huxley framework [17]. Thanks to this model, we can simulate a variety of scenarios from physiological activation to bursting patterns in different settings like sleep, the release of hormones, and certain pathological conditions [6]. In this context, bifurcation analysis helps us to identify the physiological boundary in parameter space.

Bifurcation analysis is a central technique in computational modeling for understanding the quantitative change in behavior and stability of dynamical systems. It allows one to systematically explore how changes in system parameters influence transitions between different dynamical regimes, such as resting, periodic spiking, or bursting. By identifying bifurcation points and classifying their types, one can construct a detailed map of the system's behavior across the parameter space. In neuronal models, Hopf bifurcations are especially relevant, as they mark the onset of oscillatory dynamics from a stable equilibrium and vice versa. Hopf bifurcations are classified as supercritical or subcritical depending on whether the emerging limit cycle is stable or unstable. The nature of Hopf bifurcations along such curves is characterized by the first Lyapunov coefficient (l_1). A Codim-1 bifurcation analysis—where one parameter is varied—can identify the presence of Hopf points and limit points. A Codim-2 analysis, involving simultaneous variation of two parameters, enables the tracing of Hopf curves, also known as stability boundaries, saddle-node curves, and their intersections, which serve as critical boundaries between different dynamic regimes. A change in the sign of l_1 indicates a generalized Hopf point, marking a transition between supercritical and subcritical Hopf bifurcations. Beyond oscillatory behavior, neuronal models may also exhibit multiple equilibria for the same parameter values. These multiple equilibria can merge and annihilate via saddle-node (LP) bifurcations. When two saddle-node bifurcations coalesce, a cusp point bifurcation occurs, often a key organizing center for bistability or abrupt state transitions. We can systematically perform the bifurcation analysis using numerical continuation techniques and detect bifurcation points [18].

Numerous studies have explored the bifurcation analysis of neuronal models using reduced-order models to facilitate the study of variables of interest [10, 11, 19–22]. Cressman et al. developed a reduced Barreto-Cressman model (RBC) to study the role of slow variables in bursting [2]. Although the RBC model can predict bursting, it has been found that the model is of limited use for higher values of pump strength. Also, the work by Cressman et al. was primarily focused on codim-1 and codim-2 bifurcation analysis concerning only glial uptake strength and diffusion constant, neglecting interactions between other parameters. Since the potassium current significantly influences neuronal hyperactivity [23–25], understanding the interplay between the parameters pump strength and bath potassium concentration is crucial. Following

an action potential, intracellular accumulation of [Na^+] and extracellular accumulation of [K^+] occur; the ion pump restores these gradients, and its strength determines the rate of recovery, neuronal firing patterns, and overall neuronal stability. Also, the energy consumption and metabolic cost are directly influenced by the pump's activity during gradient restoration. Malfunction of the pump can lead to pathological phenomena such as bursting, epilepsy, and ischemia. In a separate work, Barreto et al. performed the bifurcation analysis of only fast dynamics by treating slow variables as parameters, which does not provide a complete picture [3]. Subsequently, Erhardt et al. extended the bifurcation analysis to the BC model. As the focus of the study was not stability analysis, this was also limited to codim-1 bifurcations with limited exploration [26]. In both studies, bifurcation results show a hysteresis behavior (a path-dependent response), indicating the existence of multistability in the system. In both studies by Erhardt et. al. [26] and Cressman et al. [2], bifurcation points were identified, but the clear stability boundaries were not demarcated, which would provide us with a detailed picture of the different operating regions for neurons. A unified model incorporating $[K_o]^+$, $[Na_i]^+$, $[Cl_i]^-$ and $[Ca_i]^{2+}$ is needed for a complete bifurcation analysis of neural dynamics. In this work, we incorporate the $[Cl_i]^-$ equation, adopted from [17], into the Cressman model [2], and perform bifurcation analysis of the resulting unified model. In the following sections, we present a detailed bifurcation analysis of this unified Barreto–Cressman model to clarify neural dynamics and identify the control parameters governing physiological behavior.
The article is organized as follows: In Section 2, we formalize different neuronal models analyzed in this work. In Section 3, we describe the methodology adopted in the bifurcation study and the significance of different bifurcation points, and provide a brief description of the working methodologies of MatCont for bifurcation analysis and time integration [27]. Section 4 presents the results: bifurcation analysis of neural models in codim-1 and codim-2. The significance of the identified bifurcation points and their impact on the system's dynamics are discussed in detail. In Section 5, concluding remarks on the work and its implications are presented.

2 Neural models

This section introduces the system of ordinary differential equations governing neuronal dynamics. The model is based on the Hodgkin-Huxley formalism, integrated with ion dynamics and conservation principles.

2.1 Barreto-Cressman model

The BC model is one of the physiologically detailed models, which includes the dynamics of membrane action potential, gating variables, and ion concentrations. One can refer to the work of Cressman et. al. for the details of the model development [2, 3]. Here, the outward current is taken as positive, which is a standard convention. The original BC model is given as:

Table 1: Nomenclature

Variable	**Description**
V	Membrane action potential (mV)
I_{Na}	Sodium current ($\mu A/cm^2$)
I_K	Potassium current ($\mu A/cm^2$)
I_L	Leak current ($\mu A/cm^2$)
m	Gating variable for sodium activation
h	Gating variable for sodium inactivation
n	Gating variable for potassium activation
α	Forward rate constant for transition between the open-closed state
β	Backward rate constant for transition between the open-closed state
$[Ca^{2+}]_i$	Intracellular calcium concentration (Mm)
V_{Na}	Reversal potential of persistent sodium current (Mm)
V_K	Reversal potential of potassium current (mV)
$[Na^+]_o$	Extracellular sodium concentration (mM)
$[Na^+]_i$	Intracellular sodium concentration (mM)
$[Cl^-]_o$	Extracellular Chlorine concentration (mM)
$[Cl^-]_i$	Intracellular Chlorine concentration (mM)
$[K^+]_o$	Extracellular potassium concentration (mM)
$[K^+]_i$	Intracellular potassium concentration (mM)
I_{pump}	Pump current (mM/s)
I_{diff}	Potassium diffusion to the nearby bath (mM/s)
I_{Glia}	Glia uptake ((mM/s))
Acronyms	
BT	Bogdanov-Takens
CP	Cusp bifurcation
GH	Generalized Hopf bifurcation
SubH	Subcritical Hopf bifurcation
SupH	Supercritical Hopf bifurcation
LP	Limit point
LPC	Limit point of cycles
$l1$	First Lyapunov coefficient

$$
\begin{cases}
C_m \dfrac{dV}{dt} = -(I_{\mathrm{Cl}} + I_{\mathrm{Na}} + I_K), & \text{in } (0,T], \\
\dfrac{d\mathbf{y}}{dt} = \phi\big(\alpha_{\mathbf{y}} \cdot (1-\mathbf{y}) - \beta_{\mathbf{y}} \cdot \mathbf{y}\big), & \text{in } (0,T], \\
\dfrac{d[\mathrm{Ca}^{2+}]_i}{dt} = -\dfrac{[\mathrm{Ca}^{2+}]_i}{80} - g_{\mathrm{Ca}} \dfrac{0.002(V - E_{\mathrm{Ca}})}{1 + \exp\left(-\frac{25+V}{2.5}\right)}, & \text{in } (0,T], \\
\dfrac{d[\mathrm{K}^+]_o}{dt} = -I_{\mathrm{diff}} - 2\beta I_{\mathrm{pump}} - I_{\mathrm{Glia}} - 0.33 I_K, & \text{in } (0,T], \\
\dfrac{d[\mathrm{Na}^+]_i}{dt} = 0.33 \dfrac{I_{\mathrm{Na}}}{\beta} - 3 I_{\mathrm{pump}}, & \text{in } (0,T].
\end{cases}
\tag{1}
$$

where

,

$$\mathrm{E}_{Na} = 26.64\ log\left(\frac{[Na^+]_o}{[Na^+]_i}\right), E_K = 26.64\ log\left(\frac{[K^+]_o}{[K^+]_i}\right),$$

$$I_{Glia} = \left(\frac{g_{Glia}}{1+e^{\left(\frac{18-[K^+]_o}{2.5}\right)}}\right), I_{pump} = \frac{\varrho}{1+e^{(5.5-[K^+]_o)}}\left(\frac{1}{1+e^{\left(\frac{25-[Na^+]_i}{3}\right)}}\right)$$

$$I_{ClL} = g_{ClL}(V - E_{Cl}), I_K = \left(g_K \cdot n^4 + g_{AHP}\frac{[Ca^{2+}]_i}{1+[Ca^{2+}]_i} + G_{KL}\right)(V - E_K),$$

$$[K^+]_i = 158 - [Na^+]_i, [Na^+]_o = 144 - \beta([Na^+]_i - 18),$$

$$I_{diff} = \epsilon([K^+]_o - K_\infty), I_{Na} = (g_{NaL} + g_{Na} \cdot m^3 \cdot h)(V - E_{Na}).$$

Here $g_i(i = K, Na, AHP, Cl_L, K_L, Glia, Na_L)$ in $\mu F/cm^2$ are ionic channel conductance, $\mathbf{y} = [h, m, n]$ represents the gating variables, $E_i(i = Na, Cl, K)$ are reversal potentials defined in mV, capacitance C_m in $\mu F/cm^2$, currents in $\mu A/cm^2$, time t in milliseconds. The chloride ions concentration is kept fixed at $[Cl^-]_o = 130$ mM and $[Cl^-]_i = 6$ mM, which fix the chlorine reversal potential at $E_{Cl} = 26.64 \cdot log([Cl^-]_i/[Cl^-]_o)$

2.2 Reduced Barreto-Cressman model

The BC model includes two distinct time scales: slow and fast variables. By assuming that fast variables remain at their steady-state values, we can separate fast and slow dynamics. This approach allows us to reduce the original seven-variable BC model to a simplified two-variable ($[K^+]_o$ and $[Na^+]_i$) model that focuses solely on slow dynamics [2].

However, we observed that the reduction introduces a phase error into the system, so an external stimulus of $I_{ext} = 0.5\ \mu A/cm^2$ is applied for phase correction. The RBC model is expressed as follows:

$$\begin{cases} \dfrac{d[K^+]_o}{dt} = 0.33\ I_k - 14.0\ I_{pump} - I_{Glia} - I_{diff} + I_{ext}, & \text{in } (0, T], \\ \dfrac{d[Na^+]_i}{dt} = 0.04714\ I_{Na} - 3\ I_{pump} & \text{in } (0, T]. \end{cases} \tag{2}$$

where

$$[K^+]_i = 140 + (18.0 - [Na^+]_i),$$
$$[Na^+]_o = 144.0 - 7\ ([Na^+]_i - 18.0),$$

$$I_{Glia} = \frac{gGlia}{1.0 + \exp\left(\frac{18.0-[K^+]_o}{2.5}\right)},$$

$$I_{pump} = \frac{\varrho}{1.0 + \exp\left(\frac{25-[Na^+]_i}{3}\right)} \cdot \frac{1}{1.0 + \exp\left(5.5 - [K^+]_o\right)},$$

$$I_{diff} = \epsilon([K^+]_o - K_\infty),$$

$$
\begin{aligned}
I_K &= 0.94\ (g_1\ g_2\ g_3\ g_4 + g_{lk}),\\
I_{Na} &= g_1\ g_2\ g_3\ g_4 + 1.5,\\
g_3 &= \left(\frac{1.0}{1+\exp\left(35.7\left(1.0+1.94\frac{[Na^+]_i}{[Na^+]_o}-24.3\frac{[K^+]_o}{[K^+]_i}\right)\right)}\right)^5,\\
g_{lk} &= 2.6\exp\left(-32.5\frac{[K^+]_o}{[K^+]_i}\right),\\
g_4 &= \left(\frac{1.0}{1+\exp\left(0.88\left(1.0+1.48\frac{[Na^+]_i}{[Na^+]_o}-24.6\frac{[K^+]_o}{[K^+]_i}\right)\right)}\right)^5,\\
g_2 &= \exp\left(\frac{2\left(1.0-7.41\frac{[K^+]_o}{[K^+]_i}\right)}{1.94+1.98\exp\left(-2.6\frac{[Na^+]_i}{[Na^+]_o}\right)}\right),\\
g_1 &= 420.0\left(1.0-0.75\left(1.0-0.93\exp\left(-2.6*\frac{[Na^+]_i}{[Na^+]_o}\right)\right)^{0.3}\right).
\end{aligned}
$$

2.3 Unified Barreto-Cressman model

In previous formulations of the BC model, the chloride ion $[Cl^-]$ concentration was treated as a constant parameter. To further extend the framework, $[Cl^-]$ ion dynamics are incorporated into the BC framework from [17], which we refer to as the Unified Barreto-Cressman (UBC) model. $[Cl^-]$ plays a pivotal role in regulating the balance between neuronal inhibition and excitability. Low intracellular $[Cl^-]$ enhances the transmembrane chloride gradient, facilitating $[Cl^-]$ influx through inhibitory channels, which leads to membrane hyperpolarization and increased inhibitory efficacy. In contrast, elevated intracellular $[Cl^-]$ reduces or reverses the gradient, driving $[Cl^-]$ efflux, resulting in membrane depolarization and heightened excitability. Disruption of chloride homeostasis can impair inhibitory signaling, leading to neuronal hyperexcitability, which may contribute to pathological bursting and the onset of epileptic seizures. Thus, a detailed understanding of chloride dynamics is essential for uncovering the mechanisms of burst generation and their role in seizures. In the proposed UBC model, chloride ions are allowed to evolve dynamically. Remaining system variables—membrane action potential and other ionic dynamics are accordingly modified to incorporate the effects of chloride. The dynamics of the gating variables remain the same as in the BC model. The model schematic diagram is given in Figure 1, and the resulting UBC model is formulated as follows:

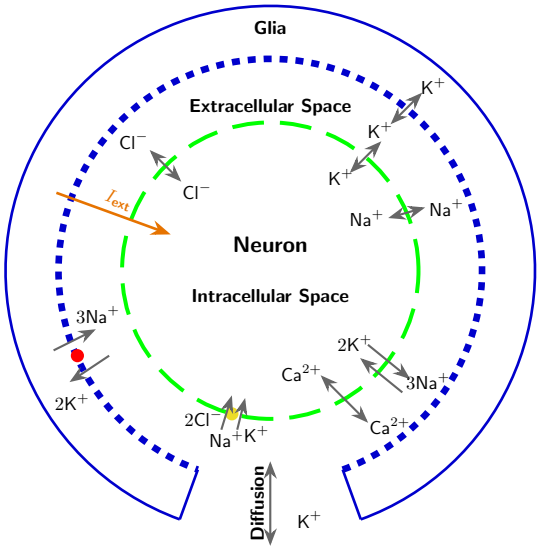

Fig. 1: Ionic fluxes in single-compartment unified Barreto-Cressman model

$$
\begin{cases}
C_m \dfrac{dV}{dt} = (-I_{Cl} - I_{Na} - I_K + I_{ext}), & \text{in } (0,T], \\
\dfrac{d[K^+]_o}{dt} = -\dfrac{1}{\tau}(I_{diff} + 14I_{pump} + I_{glia} + 2I_{gliap} - 7(I_{kcc2} + I_{nkcc1} + \gamma I_K)), & \text{in } (0,T], \\
\dfrac{d[Na^+]_i}{dt} = \dfrac{1}{\tau}(\gamma I_{Na} - 3I_{pump} - I_{nkcc1}), & \text{in } (0,T], \\
\dfrac{d[Cl^-]_i}{dt} = \dfrac{\gamma}{\tau} I_{ClL} - I_{kcc2} - 2I_{nkcc1} & \text{in } (0,T].
\end{cases} \tag{3}
$$

where

$$
I_{gliap} = \frac{1}{3}\frac{\varrho}{1+e^{(3.5-[K^+]_o)}}\left(\frac{1}{1+e^{\left(\frac{25-[Na^+]_i}{3}\right)}}\right)
$$

$$
I_{pump} = \frac{\varrho}{1+e^{(3.5-[K^+]_o)}}\left(\frac{1}{1+e^{\left(\frac{25-[Na^+]_i}{3}\right)}}\right),
$$

$$
I_{nkcc1} = \frac{U_{nkcc1}}{1+e^{(16-[K^+]_o)}}\left(log\left(\frac{[K^+]_i * [Cl^-]_i}{[K^+]_o * [Cl^-]_o}\right) + log\left(\frac{[Na^+]_i * [Cl^-]_i}{[Na^+]_o * [Cl^+]_o}\right)\right)
$$

$$I_{kcc2} = U_{kcc2} * log\left(\frac{[K^+]_i * [Cl^-]_i}{[K^+]_o * [Cl^-]_o}\right).$$

Only the modifications introduced to the BC model are presented here. The physiological range of parameters is given in Table 3.

Table 2: Parameters values

Parameters	Value	Description
ϵ	1.33 s^{-1}	Diffusion constant
ϱ	1.25 mM/s	Pump strength
K_∞	4 mM	bath potassium concentration
$gGlia$	15 mM/s	Glia uptake strength
C_m	1.0 $\mu F/cm^2$	Membrane capacitance
g_{Na}	30 mS/cm^2	Sodium conductance
g_{Ca}	0.1 mS/cm^2	Calcium conductance
g_K	25 mS/cm^2	Potassium conductance
g_{KL}	0.05 mS/cm^2	Potassium leakage conductance
g_{NaL}	0.0247 mS/cm^2	Sodium leakage conductance
g_{ClL}	0.1 mS/cm^2	Chloride leakage conductance
g_{AHP}	0.01 mS/cm^2	AHP conductance
γ	0.0445	Membrane current conversion factor
β	7	Intracellular and extracelluar volume ratio
τ	0.001	Time conversion factor (ms to s)
U_{nkcc1}	0.1 mM/s	Cotransporter strength
U_{kcc2}	0.3 mM/s	Cotransporter strength

Table 3: Physiological range of parameters

Parameters	Range	
K_∞	$(0, 50)$ mM	[3, 28]
ϵ	$(0, 3)$ s^{-1}	[2]
ϱ	$(0, 12.5)$ mM/s	[2, 29, 30]
$gGlia$	$(0, 70)$ mM/s	[31]

3 Methodology: Bifurcation analysis

In this section, a brief explanation of the bifurcation analysis is presented. The methodology is explained in terms of a general system of the form:

$$\dot{\mathbf{x}} = f(\mathbf{x}, \boldsymbol{\mu}), \quad \mathbf{x} \in \mathbb{R}^n, \ \boldsymbol{\mu} \in \mathbb{R}^k,$$

where f is a smooth vector field, $\mathbf{x}$ is the state vector of dimension n, and $\boldsymbol{\mu}$ is the parameter vector of dimension k. We analyze the system dynamics as parameters are

varied. When the bifurcation analysis is performed by varying any single parameter, it is called a codim-1 bifurcation. Similarly, when two parameters are varied simultaneously, it is called a codim-2 bifurcation. Although this is a standard procedure in bifurcation analysis, it is presented here again for the sake of completeness. The steps to perform bifurcation analysis are as follows:
Step 1: To perform the analysis, first we need to compute the equilibrium state of the system, which is determined by solving the steady-state condition:

$$f(\mathbf{x}, \boldsymbol{\mu}) = 0,$$

for a fixed value of the bifurcation parameter vector $\boldsymbol{\mu} \in \mathbb{R}^k$. However, it is quite difficult to solve it for a highly nonlinear problem like neural dynamics. The equilibrium state for the dynamical system is usually obtained via time simulation of the governing ODEs until the transient dynamics are settled and the equilibrium state is achieved. Once the equilibrium state is obtained, codim-1 analysis is performed, which is also known as "linear stability analysis".
Step 2: Next, the equilibrium curve is drawn for a range of parameters, and the eigenvalues of the Jacobian at the equilibrium points are computed. The nature of the eigenvalues decides the stability of the system. A bifurcation is detected when eigenvalues cross the imaginary axis, indicating a change in the stability of the equilibrium. Since the Jacobian formation is based on a Taylor series expansion, this study is valid only in the proximity of the equilibrium. The Jacobian matrix:

$$J(\mathbf{x}, \boldsymbol{\mu}) = \frac{\partial f}{\partial \mathbf{x}}(\mathbf{x}, \boldsymbol{\mu})$$

The saddle-node bifurcation (a single real eigenvalue crosses zero) and Hopf bifurcation (a pair of complex-conjugate eigenvalues cross the imaginary axis, leading to the emergence of a limit cycle) are the two relevant codim-1 bifurcations for neural dynamics. The numerical continuation technique is adopted to plot the solution with parameter variation and detect bifurcation points. Dynamical systems can exhibit multiple equilibrium points for the same parameter values. As a parameter varies, these equilibria can collide and disappear via a saddle-node bifurcation, also known as a limit point or fold point bifurcation.
If the first Lyapunov coefficient of the Hopf point is negative, it is a supercritical Hopf point; if the first Lyapunov coefficient is positive, it is a subcritical Hopf point. On the unstable side of the Hopf point, equilibrium points are enclosed by a stable limit cycle, resulting in oscillatory behavior. However, on the stable side of the Hopf point, the existence of the limit cycle depends on the type of Hopf bifurcation. In the case of a subcritical Hopf bifurcation, unstable limit cycles coexist around the stable equilibrium points and keep shrinking inward. In contrast, for a supercritical Hopf bifurcation, unstable equilibrium points are surrounded by a stable limit cycle. On the supercritical side, the transition from stable to oscillatory behavior is very smooth. There is no hysteresis effect when crossing the parameter threshold. We can get arbitrarily close to the supercritical bifurcation point, but not in the case of a subcritical bifurcation point. Operating on the subcritical Hopf side, firing begins abruptly. If a

perturbation stays well inside the unstable limit cycle, the neuron returns to rest; if it goes outside the unstable limit cycle, the neuron settles into a globally stable limit cycle. The neuron shows hysteresis behavior until the point where the unstable and stable limit cycles merge. Sometimes, even a small perturbation can start oscillations before the bifurcation point is reached.

Step 3: Once the Hopf bifurcation point is detected, the bifurcation of the limit cycle is carried out for the detection of bifurcation points like limit points of cycles (LPC), period doubling, and Neimark-Sacker. The stable and unstable limit cycles collide and vanish through an LPC.

Step 4: The bifurcation analysis can be extended to a two-parameter space, called codim-2 analysis. Codim-2 bifurcations occur at parameter values where two codim-1 bifurcation curves intersect or coalesce. In codim-2, the locus of codim-1 bifurcations is plotted with conditions like $\det(J) = 0$ for saddle-node bifurcations, $\mathrm{Re}(\lambda) = 0$ with $\mathrm{Im}(\lambda) \neq 0$ for Hopf bifurcations forming a stability boundary (Hopf curve). The system with two bifurcation parameters $(\mu_i, \mu_j) \in \mathbb{R}^2$ is represented as:

$$\dot{\mathbf{x}} = f(\mathbf{x}, \mu_i, \mu_j).$$

Below is the list of codim-2 bifurcation points relevant to neural dynamics:

Cusp bifurcation: when two LP curves collide tangentially and subsequently disappear, it marks the CP bifurcation point. At the CP point, the linear restoring force (Jacobian) and the quadratic nonlinear correction (its derivative) both vanish, leaving only the weak cubic nonlinearity to restore the equilibrium. This double degeneracy is what separates a normal LP curve from the CP point. The cusp bifurcation governs the bistability between two non-oscillatory states. When the system operates near the CP point, the restoring force weakens, and the system's recovery no longer follows a simple exponential decay but takes unexpectedly longer to recover from perturbation. Near the CP point, no gradual adjustment is possible, and the system shifts to a completely different state. This is the physical origin of hysteresis and the slow recovery.

Bogdanov-Takens bifurcation: It is characterized by a double zero eigenvalue of the Jacobian, indicating the intersection of saddle-node and Hopf bifurcations, and the simultaneous loss of both stability and oscillatory onset in the system. The BT point marks where the system loses two eigenvalues at once. Four curves converge tangentially at this point: saddle-node, Hopf, homoclinic (saddle-loop), and fold-of-cycles. Here, an equilibrium loses stability through two routes that normally occur separately: a saddle-node (fold) bifurcation and a Hopf bifurcation. Depending on which side of these curves it starts from, a neuron near a BT point settles into one of four regimes: a stable equilibrium with no nearby oscillation; a stable equilibrium coexisting with an unstable limit cycle from a subcritical Hopf; a stable large-period limit cycle from a homoclinic connection; or loss of the equilibrium via saddle-node collision, leaving only large-scale dynamics. Since up to four curves converge at one BT point, a neuron whose parameters drift slowly through this region — via modulatory changes, adaptation currents, or shifting ion concentrations — can pass through several firing regimes in quick succession: silence, single action potential, slow oscillation, then faster periodic firing, all within a small parameter range. Which sequence occurs, and where transitions happen, depends sensitively on the exact path taken, making firing onset

strongly history- and path-dependent. The trajectory near a BT point shows a distinctive slow-fast-slow shape: a slow departure from rest (weak linearized dynamics), a fast active phase once the fast nonlinearity dominates, and a slow return via the weakened linear dynamics near the saddle.

generalized Hopf bifurcation: At the GH point, two parameters act together: one controls the axis crossing of the eigenvalues, and the other controls the change in the sign of the first Lyapunov coefficient (l_1). A point on the Hopf curve at which l_1 vanishes, indicating a transition of Hopf bifurcations from subcritical to supercritical or vice versa. Since $l_1 = 0$ at the GH point, the higher-order coefficient l_2 comes into play and determines the dynamics. Depending on which side of the GH point the system is on, supercritical or subcritical behavior determines how the neuron begins to fire. At GH, a stable equilibrium and a stable large-amplitude oscillation coexist simultaneously, separated by an unstable cycle that acts as a threshold, giving rise to bistable characteristics [18]. In this work, `MatCont` is used for the bifurcation study of neuronal dynamics. `MatCont` is a MATLAB(R)-based continuation package specifically designed for the bifurcation analysis of dynamical systems [27]. `MatCont` supports codim-1 and codim-2 bifurcations, continuation of equilibrium and periodic orbits, tracing stability boundaries, and automatic classification of bifurcation types. Specifically, it traces an equilibrium curve and evaluates the test function proportional to the determinant of the system Jacobian at each point; if the test function changes sign, the code flags a bifurcation. Once a bifurcation is detected, `MatCont` uses a bisection method to find the exact location of the bifurcation point. Further, it computes the eigenvalues to label these points as stable or unstable, and based on the eigenvalues, labels them as limit point, Hopf, limit point of cycles, Bogdanov-Takens, generalized Hopf, or cusp bifurcation. Next, if the system is unstable, a limit cycle will be generated, and the first Lyapunov coefficient is computed to decide whether the new limit cycle is stable or unstable.

As mentioned earlier, due to the presence of multiple time scales, the system of equations represented in Equations (1), (2), (3) is a highly stiff system, which makes it computationally expensive to solve using simple explicit time integrators such as Runge–Kutta methods or the Euler method due to their conditional stability. To ensure convergence and computational efficiency, the numerical integration of the governing system of differential-algebraic equations (DAEs) is performed using `ode15s`, a built-in MATLAB solver. It is both time-adaptive and order-adaptive, using local truncation error and the required accuracy to adjust the time step and integration order adaptively. Since `ode15s` is an implicit method, the time step is determined by the desired solution accuracy through adaptive error control, rather than by stability constraints. Moreover, it possesses A-stable (or nearly A-stable for higher-order formulas) stability characteristics. As an implicit method, the next-step solution is obtained by solving a nonlinear system of algebraic equations using Newton iterations, which involve computationally expensive Jacobian assembly and linearized system solution. Nevertheless, because large time steps can be taken without compromising stability, this method significantly reduces overall computational time. Furthermore, to minimize computational cost, `ode15s` updates the Jacobian only when there is a significant change in the time step or when Newton iteration fails. The functional parameters

for `ode15s` remain at their default values with relative tolerance of 10^{-3}, absolute tolerance of 10^{-6}, and a maximum step size equal to 10% of |start time − end time|

4 Results and Discussions

In this section, a comparison between the RBC and BC models and the bifurcation analysis of the RBC, BC, and UBC models concerning various parameters are presented. Further, the time evolution of neuronal dynamics near identified bifurcations is presented and discussed.

4.1 A comparison of the RBC model and BC model

In this section, the bifurcation results from the RBC model are compared with the BC model. Generally, we are interested in the amplitude and spike time of the membrane action potential; since the RBC model does not include the membrane action potential as a state variable, $[K^+]_o$ is selected instead to enable a one-to-one comparison between the two models.

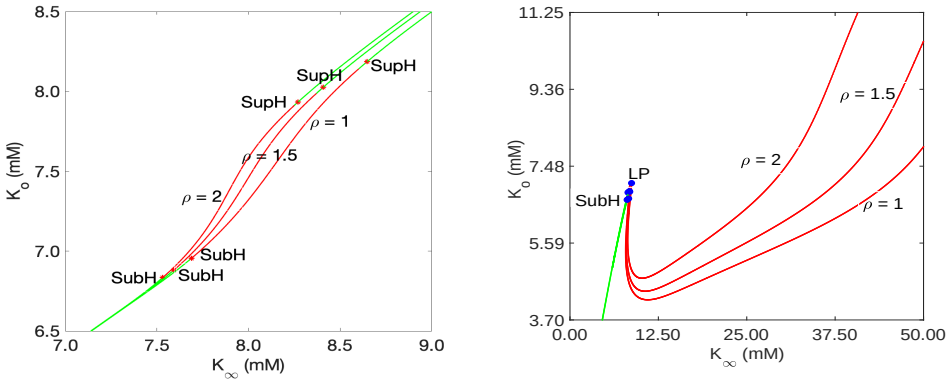

(a) (b)

Fig. 2: A comparison of the bifurcation plot between (a) RBC and (b) BC for K_∞, for different values of $\varrho = (1, 1.5, 2)\ mM/s$, and fixed $\epsilon = 1.25\ s^{-1}$ and $gGlia = 66\ mM/s$. In the plots, green curves represent stable equilibrium and red curves represent unstable equilibrium. Different regions and important bifurcation points are marked.

As we can see in Figure 2, for a lower value of pump strength (ϱ), both models predict bifurcation points close to each other. However, while the BC model detects

two saddle-node bifurcation points, no saddle nodes are detected in the RBC model. For $\varrho = 1\ mM/s$, the RBC model predicts that K_o reaches a depolarized state once K_∞ exceeds 8.6 mM, whereas the BC model indicates that $[K^+]_o$ never stabilizes for physically plausible upper values of K_∞, which is 50 mM, suggesting that under realistic conditions, neurons will remain in an oscillatory state for higher values of K_∞ and never attain the stationary state.

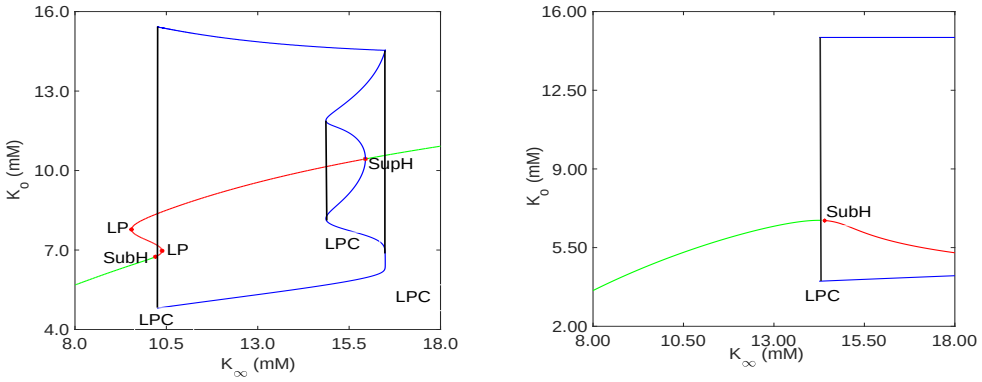

(a) (b)

Fig. 3: A comparison of the bifurcation plot for K_∞ between (a) RBC and (b) BC for the fixed values of $\varrho = 2\ mM/s, \epsilon = 0.25\ s^{-1}, gGlia = 66\ mM/s$. In the plot, solid blue curves represent the limit cycle. Limit points of cycles, unstable equilibrium, and stable equilibrium are represented by black vertical lines, red curve, and green curve, respectively.

For comparison of RBC and BC, a set of parameters $\varrho = 2\ mM/s, \epsilon = 0.25\ s^{-1}$, $gGlia = 66\ mM/s$ is chosen. We can see in Figure 3a that in the range of $K_\infty = [9, 18]$ mM, the RBC model undergoes two Hopf bifurcations and two saddle-node (LP) bifurcations, whereas the BC model shows only one Hopf bifurcation. The detection of Hopf bifurcation points indicates that the neuron is entering an oscillatory regime and will show limit cycles. The maximum and minimum values of the oscillations' amplitude are plotted in blue in Figure 3. In Figure 3a, we can see that below $K_\infty = 10.2\ mM$, the neuron is in stable equilibrium or returns to a stable equilibrium, even if the initial state is far away from equilibrium. After $K_\infty = 10.2\ mM$, the neuron enters an oscillatory regime via a subcritical Hopf bifurcation. This transition from equilibrium to oscillation is very fast, and the region of transition appears as a straight

line. This oscillatory behavior continues till $K_\infty = 16.43\ mM$. After $K_\infty = 16.43\ mM$, the neuron enters a depolarization region via a supercritical Hopf bifurcation, which means there is no change in the slow variables $[K^+]_o$ and $[Na^+]_i$. When the limit cycle is drawn from the supercritical Hopf point $K_\infty = 15.94\ mM$, with a decrease in K_∞, the limit cycle is initially stable with growing amplitude till it reaches the limit point of cycles (LPC) at $K_\infty = 14.83\ mM$. At this point, the limit cycle changes direction, becomes unstable, and continues until it reaches another LPC at $K_\infty = 16.43\ mM$. Subsequently, it reverses direction again and merges into a globally stable limit cycle coming from the left. Between $K_\infty = 15.94\ mM$ and $K_\infty = 16.43\ mM$, the neuron exhibits two stable solutions, one equilibrium and one stable limit cycle, indicating that there exists an unstable limit cycle between them. Depending on the initial guess provided, the neuron can settle into either of these two stable solutions. Beyond the LPC at $K_\infty = 16.43\ mM$, neurons show global stability in ion concentrations. In between two LPCs at $K_\infty = 14.83\ mM$ and $K_\infty = 16.43\ mM$, neurons show multi stability. In contrast, the BC model does not exhibit such dynamics within this range of $K_\infty = 8 - 18\ mM$. Specifically, no supercritical Hopf bifurcation is observed; hence, there is no shrinking or annihilation of the limit cycle. Notably, the computed value of K_o at the unstable equilibrium using the RBC model is higher than that of the BC model. We found that the amplitude of oscillation for K_o in the RBC and BC models is comparable. In conclusion, we can say that the RBC model becomes less effective as we operate neurons with strong ϱ and higher K_∞.
Next, we compare the time evolution of $[K^+]_o$ and $[Na^+]_i$ in two different regions identified from bifurcation analysis at $K_\infty = 11\ mM$ and $17\ mM$. At $K_\infty = 11\ mM$ (see Figure 4a), we observe that the RBC model exhibits oscillatory behavior. In contrast, under the same K_∞ value and initial conditions, we see in Figure 4b that the BC model displays stationary behavior. When we plot the membrane action potential (see Figure 5) over 100 seconds. It is observed that for most of the time, the neuron remains in the silent phase, and for a very brief time between 48.5 and 54.8 seconds, it shows oscillatory behavior. When we zoomed in on the plot, we can see that neurons show high-frequency oscillations. For $K_\infty = 17\ mM$, which lies beyond the LPC (see Figure 3a), the RBC predicts that the ion concentrations $[K^+]_o$ and $[Na^+]_i$ are in a depolarized state and show no oscillations, and the corresponding time evolution shown in Fig. 4a confirms this behavior. In contrast, in Figure 3b at $K_\infty = 17\ mM$, we can see that the BC model exhibits oscillatory behavior, which is confirmed by the time simulation presented in Figure 6b. We can see there is a notable discrepancy in the time evolution of both models. At higher values of K_∞, the RBC model ceases to show oscillatory behavior beyond $K_\infty = 16.43\ mM$, whereas the BC model continues to exhibit oscillations. The time evolution of FBC is presented in Figure 7, where it is observed that the neuron is in a periodic spiking state.

Based on the comparison of the bifurcation diagrams and time evolution of ion concentrations between the two models, we can conclude that the RBC model is only valid when neurons are operating at lower values of ϱ and higher g_{Glia}. For higher values of ϱ and K_∞, the RBC model fails to capture the dynamics and becomes

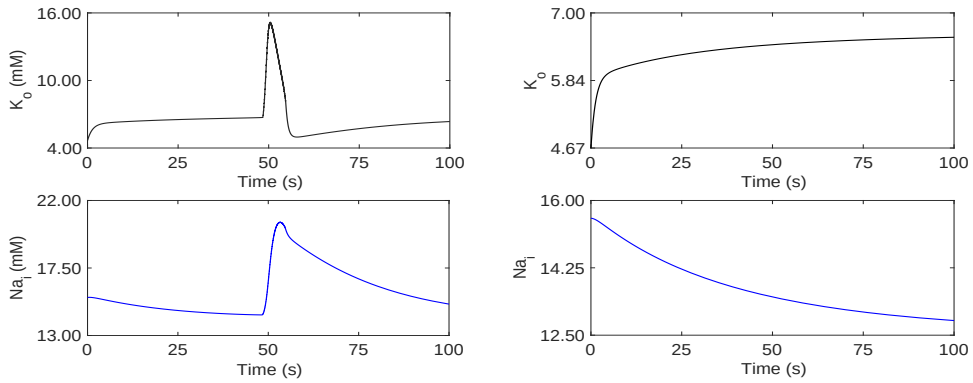

(a) (b)

Fig. 4: Time simulation of the BC model showing $[K^+]_o$, and $[Na^+]_i$. Figure 4a represents the RBC model showing oscillatory behavior, which is characteristic of bursting, and Figure 4b represents the BC model showing stationary behavior. Plots are made for $K_\infty = 11\ mM, \varrho = 2\ mM/s, \epsilon = 0.25\ s^{-1}, gGlia = 66\ mM/s$.

ineffective. To get more accurate results, the subsequent analysis is focused exclusively on the UBC model in high ϱ and low g_{Glia}.

4.2 Bifurcation analysis with respect to bath potassium K_∞

This section presents the bifurcation results of the UBC model with respect to K_∞. The analysis starts by computing the equilibrium state for a physiologically relevant parameter: $\varrho = 2\ mM/s, \epsilon = 1.33\ s^{-1}, g_{Glia} = 15\ mM/s$, and $K_\infty = 5\ mM$. Here, low g_{Glia} values are considered in the analysis to maintain the neurons in an oscillatory state. Indeed, high g_{Glia} quickly clears out the extracellular potassium, driving the neuron to the equilibrium. The resulting equilibrium state values are $V = -69.13$ mV, $m = 0.0095$, $h = 0.9976$, $n = 0.0265$, $[K^+]_o = 4.6685$ mM, $[Na^+]_i = 15.5376$ mM, $[Cl^-]_i = 4.6225$ mM, and $[Ca^{2+}]_i = 0.0$ mM. Starting from the equilibrium state, using the continuation technique, we draw the equilibrium curve between the membrane action potential and K_∞.

The resulting bifurcation plot is shown in Figure 8, where red segments denote regions of unstable equilibrium, and green segments indicate stable equilibrium. The bifurcation points and their corresponding characteristics are summarized in Table 4. With an increase in K_∞, the neuron enters an oscillatory state via Hopf bifurcation at $K_\infty = 6.57\ mM$. At $K_\infty = 6.57\ mM$, the first Lyapunov coefficient $l_1 = 0.047$

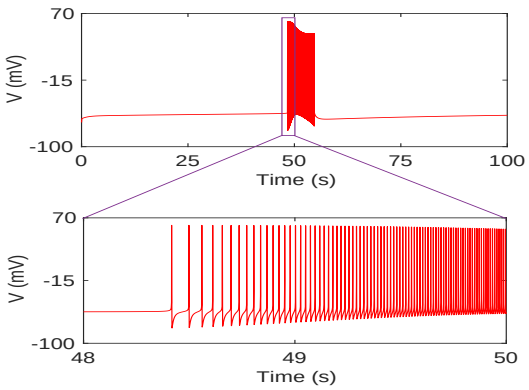

Fig. 5: Evolution of membrane action potential with zoom-in near the spike-triggered

confirms it is a subcritical Hopf bifurcation. From this subcritical Hopf point, an unstable limit cycle emerges in the direction of the stable equilibrium. With an increase in K_∞, the equilibrium curve changes its direction with a limit point bifurcation at $K_\infty = 6.58\ mM$. By further extending the equilibrium curve, the neuron shows another limit point bifurcation at $K_\infty = 1.84\ mM$. Finally, neurons enter the stationary state via a supercritical Hopf bifurcation at $K_\infty = 27.53\ mM$, and the oscillations disappear. At $K_\infty = 27.53\ mM$, the first Lyapunov coefficient is $l_1 = -0.006$, signifying a supercritical Hopf bifurcation, where the system remains stable and converges to a non-oscillatory depolarized state. In these regimes, even with initial conditions far from the equilibrium, the neuron reliably returns to equilibrium, highlighting the robustness of the stable attractor. In the bifurcation plots, blue curves denote the maximum and minimum values of the limit cycles. Since the Hopf bifurcation at $K_\infty = 27.53\ mM$ is supercritical, a stable limit cycle emerges towards the oscillatory side and persists until it terminates at a limit point of cycles at $K_\infty = 6.52\ mM$.

Table 4: List of bifurcation points shown in Figure 8

Bifurcations	$K_\infty\ (mM)$	l_1
SubH	6.57	0.05
LP	6.58	-
LP	1.84	-
SupH	27.53	- 0.01
LPC	6.55	-

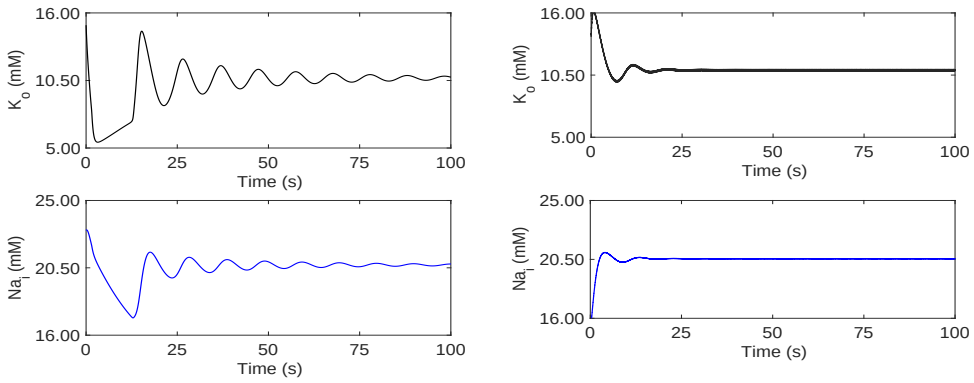

(a) (b)

Fig. 6: Time simulation of the BC model showing $[K^+]_o$, and $[Na^+]_i$, Figure 6a represents the RBC model shows stationary behavior, and 6b represents the BC model shows small amplitude oscillations. Plots are made for ($K_\infty = 17\ mM, \varrho = 2\ mM/s, \epsilon = 0.25\ s^{-1}, g_{Glia} = 66\ mM/s$)

To illustrate neuronal behavior around these bifurcation points, two representative values of K_∞ are selected: $K_\infty = 5\ mM$ (below the subcritical Hopf point) and $K_\infty = 6.52\ mM$ (after the subcritical Hopf point). The corresponding dynamical trajectories are shown in Figures 9a, and 9b, for $K_\infty = 5\ mM$, and Figures 10a, and 10b, for $K_\infty = 6.52\ mM$. As expected, at $K_\infty = 5\ mM$, the neuron remains in a stationary regime, with the membrane action potential and ion concentrations converging to fixed values regardless of the initial conditions. In contrast, after a subcritical Hopf point at $K_\infty = 6.52\ mM$, the neuron exhibits sustained oscillations, and the ion concentrations evolve along a stable limit cycle rather than settling to an equilibrium state. This illustrates how a small change in K_∞ from 5 mM to 6.52 mM can induce a qualitative transition in neuronal behavior, from a resting state to oscillatory dynamics.

From Figure 8a, we see that increasing the bath potassium concentration gradually reduces the action potential amplitude, eventually leading to a depolarized state after a supercritical Hopf bifurcation at $K_\infty = 27.53$ mM. An increase in extracellular potassium reduces the potassium reversal potential, impairing the neuron's ability to repolarize and thereby enhancing excitability. Potassium accumulation leads to membrane depolarization; depolarized neurons fire, and firing causes further potassium efflux, creating a positive feedback loop that can ultimately trigger bursting and may lead to seizures.

Figure 8b shows how the period of oscillations varies with K_∞. At low K_∞, the period increases sharply, evident from the near-vertical slope of the curve, indicating

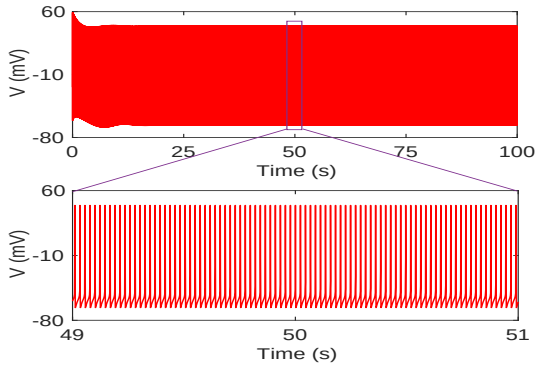

Fig. 7: Evolution of membrane action potential with zoom-in between 49 and 51 seconds

low-frequency activity and a transition to a silent phase. Since neurons should remain in an oscillatory regime under normal physiological conditions, such low values of bath potassium concentration are not suitable, as oscillations die out. At the other extreme, high K_∞ leads to very short periods and excessively high-frequency oscillations, before pushing neurons toward a depolarized state. A physiologically desirable operating range lies between two Hopf points, where the neurons are in oscillatory phase.

4.3 Bifurcation analysis with respect to external current I_{ext}

In this section, the bifurcation analysis of the UBC model with respect to the external current I_{ext} is presented. Figure 11a shows the membrane action potential at equilibrium as a function of I_{ext}, along with the corresponding bifurcation points. The analysis reveals two Hopf bifurcations: a subcritical Hopf at $I_{ext} = 1.04\ \mu A/cm^2$, and a supercritical Hopf at $I_{ext} = 39.92\ \mu A/cm^2$. As in the earlier case, in Figure 11a, red segments of the diagram indicate regions of unstable equilibrium, while green segments correspond to a stable equilibrium solution. For parameter values, $K_\infty = 5\ mM, \varrho = 1.25\ mM/s, glia = 15\ mM/s$ and $\epsilon = 1.33\ s^{-1}$, the neuron shows a subcritical Hopf bifurcation at $I_{ext} = 1.04\ \mu A/cm^2$ and enters into oscillatory state. With an increase in I_{ext}, the equilibrium curve changes its direction via an LP bifurcation at $I_{ext} = 1.053\ \mu A/cm^2$. This trend continues until the neuron undergoes another change in direction via another LP bifurcation at $I_{ext} = -12.1\ \mu A/cm^2$. Since all plots are restricted to the physiological range and $I_{ext} = -12.1\ \mu A/cm^2$ is not in the physiological range, this LP point is not shown in the plot. Finally, neurons enter a stationary state through the supercritical Hopf bifurcation at $I_{ext} = 13.87\ \mu A/cm^2$, and cease to show oscillatory behavior. Since the second Hopf bifurcation is supercritical, a stable limit cycle emerges towards the unstable side of the plot. The oscillations keep

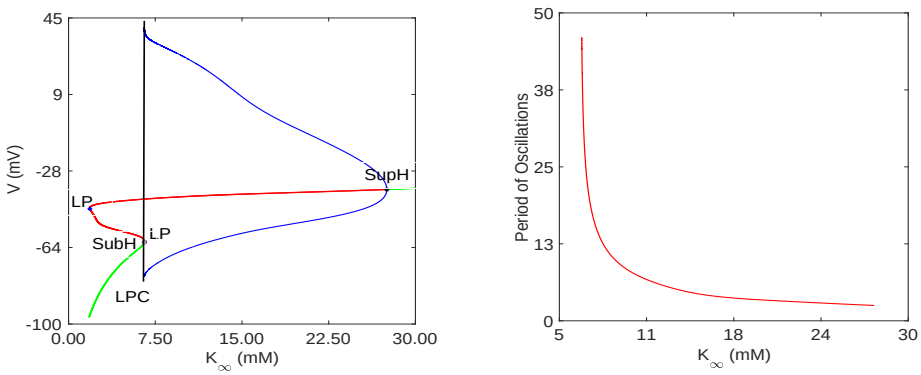

(a) (b)

Fig. 8: (a) represents the bifurcation diagram for the UBC model as a function of K_∞. All other parameters are kept fixed at their physiological values: $\varrho = 1.25\ mM/s, \epsilon = 1.33\ s^{-1}, gGlia = 15\ mM/s$. The red curve represents unstable equilibria, the green curve represents stable equilibria, and the blue curve represents the amplitude of oscillations. (b) represents the period of oscillations with respect to K_∞.

growing in amplitude till it reaches LPC at $I_{ext} = 0.89\ \mu A/cm^2$. After this, the limit cycle reverses its direction and merges with an unstable limit cycle emerging from a subcritical Hopf bifurcation point. The transition from an unstable limit cycle to a stable limit cycle happens in a very short range of I_{ext}, which appears as a straight line in Figure 11b. The blue curves in Figure 8a represent the maximum and minimum amplitudes of the limit cycles, highlighting the extent of the oscillatory regimes. We can see in the plot that the amplitude of oscillations keeps decreasing till it reaches the supercritical Hopf bifurcation point at $I_{ext} = 39.06\ \mu A/cm^2$, and eventually dies out before reaching the depolarization state, indicating that I_{ext} is an important parameter to control the birth and attenuation of oscillations as well as amplitude.
Figure 12 shows the variation in the time period of oscillations with I_{ext}. For low I_{ext}, the time period is very high, implying low frequency and a sudden transition to a silent phase. Under physiological conditions, neurons should always oscillate; such low values of stimulus are of no use when neurons are in a silent state or show low-frequency oscillations. At the other end, for high I_{ext}, time periods are small, so high-frequency oscillations drive the condition towards a depolarized state. We should always operate in an oscillating region between two Hopf points.

In the above Figure 14 and Figure 13, the time evolution of neuronal dynamics around bifurcation points is presented. Two representative points $I_{ext} = 1.2\ \mu A/cm^2$ (below the subcritical Hopf point) and $I_{ext} = 1.323\ \mu A/cm^2$ (after the subcritical Hopf point) are selected. The corresponding dynamical trajectories are shown

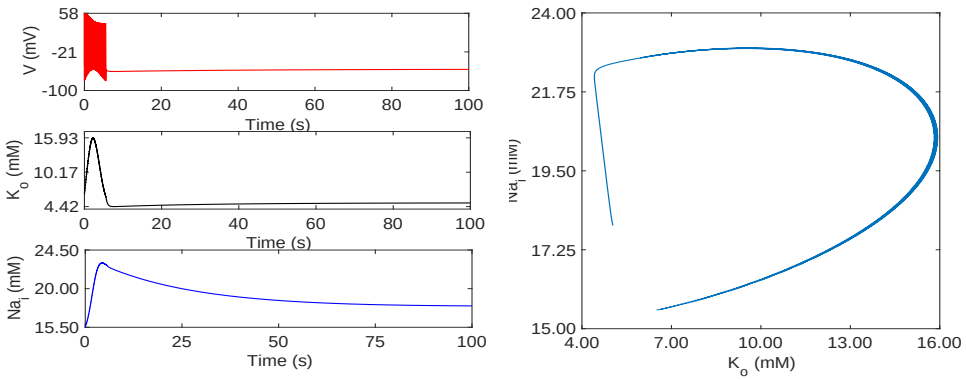

(a) (b)

Fig. 9: Time evolution of neuronal dynamics in the stationary region before the SubH point $K_\infty = 4\ mM, \varrho = 1.25\ mM/s, \epsilon = 1.33\ s^{-1}, glia = 15\ mM/s$. In Figure 9a, the evolution of the membrane action potential V, $[K^+]_o$, and $[Na^+]_i$ is shown. In Figure 9b, the phase plot of $[K^+]_o$ vs $[Na^+]_i$ is represented.

in Figures 13a, and 13b, for $I_{ext} = 1.2\ \mu A/cm^2$, and Figure 14a, and 14b, for $I_{ext} = 1.32\ \mu A/cm^2$ is presented. As expected, at $I_{ext} = 1.2\mu A/cm^2$, the neuron shows stationary behavior, with the membrane action potential and ion concentrations converging to fixed values irrespective of the initial conditions provided. In contrast, after a subcritical Hopf point at $I_{ext} = 1.32\ \mu A/cm^2$, the neuron exhibits sustained oscillations, and the ion concentrations evolve along a stable limit cycle rather than settling to an equilibrium state. This illustrates how a small change in I_{ext} from $I_{ext} = 1.2\ \mu A/cm^2$ to $I_{ext} = 1.32\ \mu A/cm^2$ can induce a qualitative transition in neuronal behavior, from a resting state to oscillatory dynamics.

4.4 Stability boundary in the $K_\infty - \varrho$ plane

Codim-2 bifurcation analysis helps us to draw a stability boundary with simultaneous variation of two parameters. Here, the stability boundary is traced in the $K_\infty - \varrho$ parametric space. As shown in Figure 15, this two-parameter exploration reveals the presence of three generalized Hopf bifurcation points, one Bogdanov–Takens bifurcation point, and one cusp bifurcation point. In the plot, the Hopf curve is represented in blue color, and the limit point curve is represented in green color. At each generalized Hopf point, the first Lyapunov coefficient changes sign, dividing the Hopf curve into regions corresponding to supercritical and subcritical bifurcations.

The presence of a generalized Hopf point indicates a transition like the Hopf bifurcation, from supercritical, where a stable limit cycle emerges, to subcritical, where

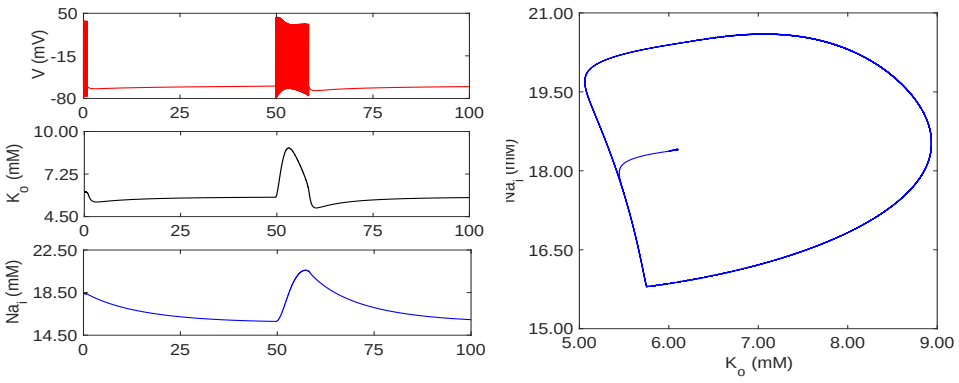

(a) (b)

Fig. 10: Time evolution of neuronal dynamics in the oscillatory region after the subcritical Hopf bifurcation point identified from a codim-1 bifurcation with respect to K_∞. Parameters : $K_\infty = 6.54\ mM, \varrho = 1.25\ mM/s, \epsilon = 1.33\ s^{-1}, gGlia = 15\ mM/s$), In Figure 10a, the evolution of membrane action potential, $[K^+]_o$ and $[Na^+]_i$ is shown. In Figure 10b, the phase plot of $[K^+]_o$ vs $[Na^+]_i$ is represented.

an unstable limit cycle appears, or vice versa. This switches the neurons from continuous firing to bistable bursting. In the $K_\infty - \varrho$ plane, the region enclosed between the two Hopf curves corresponds to the oscillatory regime, while regions outside the curves represent the stationary regime. The neuron exhibits multistability within this narrow parameter region between these three generalized Hopf points. For low values of K_∞, the system remains in a quiescent state with no neuronal firing, regardless of the magnitude of ϱ. As K_∞ increases to intermediate values, the neuron begins to exhibit oscillatory behavior, indicating the emergence of rhythmic activity. However, within the same intermediate range of K_∞, if ϱ is sufficiently low, the neuron does not fire and instead returns to a stationary state. This highlights the critical interplay between K_∞ and ϱ in governing the transition between resting and oscillatory regimes. For example, at $K_\infty = 10\ mM$, the neuron displays both stationary and oscillatory behavior depending on the value of ϱ: it remains at equilibrium for $\varrho < 0.05\ mM/s$, while oscillations emerge for $\varrho \geq 0.05\ mM/s$. For a fixed ϱ, increasing K_∞ leads to a sequence of dynamical transitions: the neuron initially remains at rest, then enters an oscillatory regime, and ultimately transitions into a depolarized state at higher K_∞ values. This progression delineates three distinct functional regimes: quiescent, oscillatory, and depolarized. In Figure 15, for a fixed value of K_∞ in the range of (11.07–13.06) mM, the neuron undergoes three successive Hopf bifurcations. Initially, the system transitions from a stationary regime to an oscillatory regime via the first Hopf bifurcation. It then returns to a stationary regime through

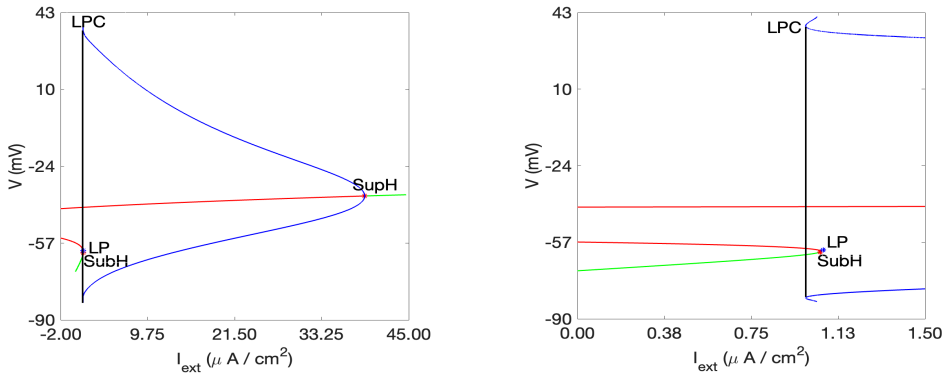

(a) (b)

Fig. 11: The bifurcation diagram of the membrane action potential V as a function of the external stimulus current I_{ext}, for parameters $K_\infty = 5\ mM, \varrho = 1.25\ mM/s, \epsilon = 1.33\ s^{-1}$, and $gGlia = 15\ mM/s$. The diagram illustrates the transition between quiescent and oscillatory states as I_{ext} varies. Figure 11b represents a zoomed-in bifurcation diagram of the UBC model near the subcritical Hopf bifurcation. The diagram distinguishes between silent and oscillatory phases. Stable equilibria are shown in green, unstable equilibria in red, and periodic orbits in blue.

a second Hopf bifurcation, followed by a re-entry into an oscillatory regime through a third Hopf bifurcation. Notably, between the second and third Hopf points, a limit point of cycles occurs at $\varrho = 0.055\ mM/s$, indicating a region of bistability or amplitude modulation in the oscillatory regime. Further, a cusp bifurcation is detected at $\varrho = 0.05\ mM/s, K_\infty = 7.86\ mM$, where two LP curves intersect. The cusp point serves as a critical threshold separating physiological and pathological behavior. Below the cusp, the neuron operates within a normal physiological range, while beyond it, the system enters a pathological state characterized by sustained depolarization. A Bogdanov-Takens point is detected at $\varrho = 0.82\ mM/s, K_\infty = 2.80\ mM$, at the intersection of the saddle-node and Hopf curves. For such a low value of $K_\infty = 2.80\ mM$, neurons never reach the firing state at this Bogdanov-Takens point. A comprehensive list of the detected codim-2 bifurcation points, along with their associated parameter values, is provided in Table 6.

Next, we investigate the temporal evolution of the membrane action potential, extracellular potassium concentration, and intracellular sodium concentration.

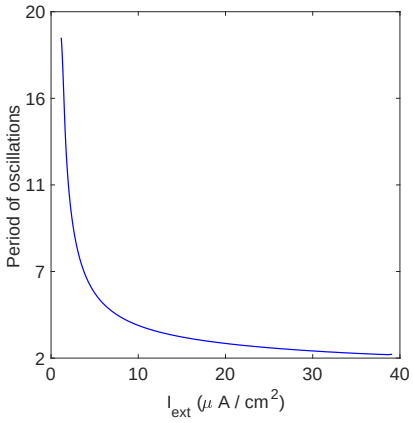

Fig. 12: Time period of oscillations

Table 5: Bifurcation points concerning I_{ext}

Bifurcations	$I_{ext}(\mu A/cm^2)$	l_1
SubH	1.05	0.03
LP	1.06	-
LP	-12.10	-
SupH	39.06	- 0.01
LPC	0.89	-

Table 6: Bifurcation points in $K_\infty - \varrho$ plane

Bifurcations	ϱ (mM/s)	K_∞ (mM)
CP	0.05	7.86
BT	0.82	2.80
GH	0.06	13.31
GH	0.06	11.07
GH	0.03	13.06

4.4.1 Time evolution near GH point at $\varrho = 0.06\ mM/s$, $K_\infty = 13.31\ mM$

The time evolution of the membrane action potential, extracellular potassium concentration, intracellular sodium, and the phase plot in the $[K^+]_o - [Na^+]_i$ plane are shown in Figures 16. We can see that the membrane potential shows low fixed-amplitude oscillations in a subthreshold band between $V = -55\ mV$ and $V = -53\ mV$, not a full action potential. The membrane action potential is locked into a periodic orbit. With some initial transient K_o settled to a practically fixed value near $(K_o = 10\ mM)$ and $(Na_i = 37.12\ mM)$. We observe the same behavior in the phase plot (see Figure16b). The slow dynamics of ions are pushing the neurons to an oscillatory state, but not strong enough to generate a full action potential, and ion clearance is slow. Neurons are operating right on the edge of the supercritical side of the GH point; a strong

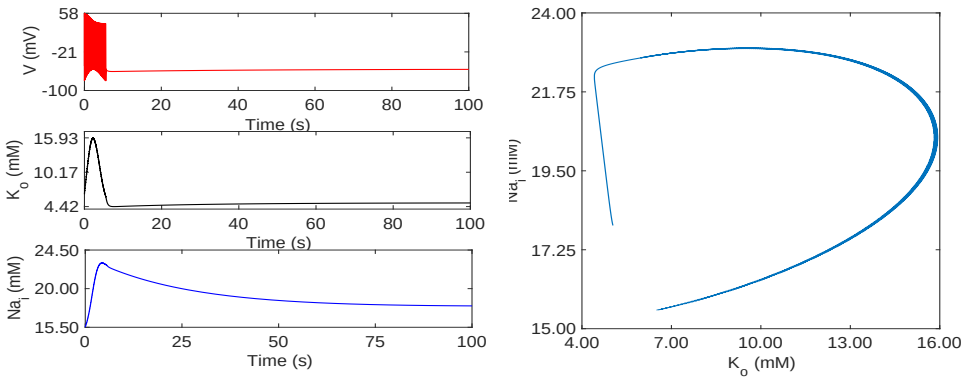

(a) (b)

Fig. 13: Time evolution of the UBC model in the stationary regimes. The stationary regime corresponds to $I_{\text{ext}} = 1.2\ \mu A/cm^2$ before the subcritical Hopf bifurcation. Parameters are fixed at $K_\infty = 5\ mM, \varrho = 1.25\ mM/s, \epsilon = 1.33\ s^{-1}$, and $gGlia = 15\ mM/s$. Figure 13a show the time courses of the V, $[K^+]_o$, and $[Na^+]_i$. Figure 13b represents the phase-plane trajectory of $[K^+]_o$ vs $[Na^+]_i$ under the same conditions as Figure 10a, illustrating the settling to a stationary point.

enough perturbation could push neurons into a full seizure, but on their own they keep recovering. With a decrease in K_∞, oscillations will grow to full action potentials. This behavior represents a pathological condition in which the neuron exhibits low-amplitude oscillations and fails to generate normal action potentials. Such a regime is undesirable and should be avoided. In the case of the second generalized Hopf point at $\varrho = 0.059\ mM/s, K_\infty = 11.07\ mM$, the neurons should exhibit the same behavior as in the case of the generalized Hopf point at $\varrho = 0.06\ mM/s, K_\infty = 13.31\ mM$, with small variations in ion concentrations and membrane action potentials.

4.4.2 Time evolution near GH point at $\varrho = 0.025\ mM/s$, $K_\infty = 13.06\ mM$

Next, the neuron is simulated near the generalized Hopf point at $\varrho = 0.025\ mM/s$ and $K_\infty = 13.06\ mM$, and the results are presented in Figures 17a and 17b. The figure illustrates that a neuron is operating near a critical point between normal excitability and depolarization. Under this parameter regime, the action potentials are progressively suppressed, and the neuron exhibits a series of small-amplitude bursts between $-55\ mV$ and $-45\ mV$, too small to be considered an action potential. Operating at low pump strength is the main reason behind such a low amplitude of oscillations.

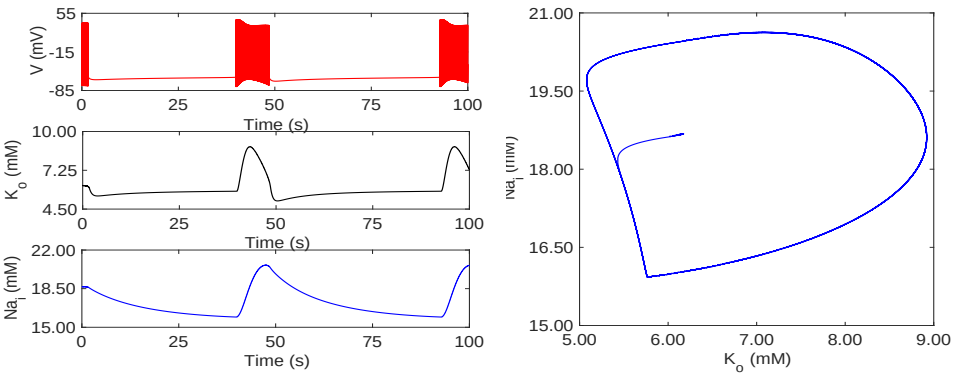

(a) (b)

Fig. 14: Temporal evolution of the UBC neuronal model in the oscillatory regime just beyond the subcritical Hopf bifurcation point, with $I_{\text{ext}} = 1.32\ \mu A/cm^2$. The parameters are set to $K_\infty = 5\ mM, \varrho = 1.25\ mM/s, \epsilon = 1.33\ s^{-1}$, and $gGlia = 15\ mM/s$. In Figure 14a, the evolution of membrane action potential, $[K^+]_o$ and $[Na^+]_i$ is shown. Figure 14b represents the phase-plane trajectory of $[K^+]_o$ versus $[Na^+]_i$, illustrating the stable limit cycle characteristic of the oscillatory regime following the subcritical Hopf bifurcation.

There is a slow buildup of K_o, reaching about 9.8 mM, a classic seizure trigger, followed by a rapid reset and repolarization. The rise in K_o strengthens pump current until it overcomes the depolarizing force, pushing the cell back toward repolarization. Since this generalized Hopf point is surrounded by a silent regime, with a very small oscillatory region, the neuron alternates between a silent phase and a period of rapid, high-frequency oscillations, referred to as bursting. During each burst, there is a sharp depolarization followed by a sequence of rapid oscillations. This is then followed by a return to the silent phase, where the membrane action potential remains near a resting value before the next burst occurs. All three variables V, K_o, Na_i oscillate in phase, a signature of slow-fast limit-cycle behavior. Figure 17b shows the asymptotic behavior of a neuron in $K_o - Na_i$ space. The dynamics settle onto a small-amplitude stable limit cycle, consistent with supercritical dynamics near a GH point. The radius of the limit cycle stays constant, confirming that the oscillation is a stable periodic attractor, a "seizure attractor" coexisting with the stable resting equilibrium. The plot indicates that, under these conditions, the system exhibits increased bursting activity, with approximately 16 bursts occurring over a 100-second interval.

In Figure 17b, the limit cycle is visibly elongated in two opposite directions, which can be attributed to the location of the generalized Hopf point. Around this point, only a narrow region exhibits oscillations, leading to rapid oscillations. The generalized Hopf

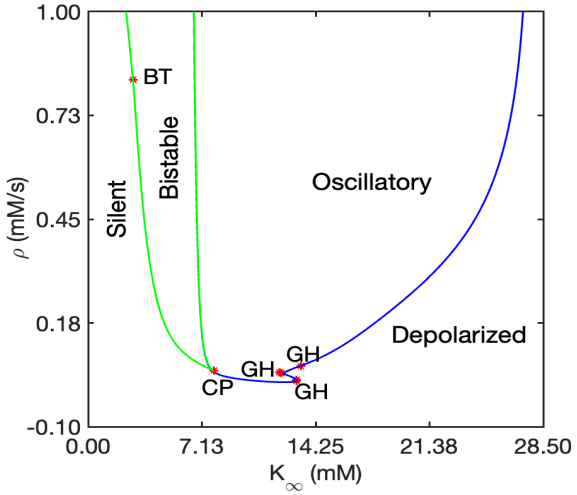

Fig. 15: Codim-2 bifurcation and the stability boundary in $K_\infty - \varrho$ space; the region between LP curves (green curves) is a bistable region; the region between Hopf curves (blue curves) is oscillatory, and outside the Hopf curves, neurons are in equilibrium

point is predominantly surrounded by stable and stationary regions, which constrain the dynamics to the observed limit cycle shape.

4.4.3 Time evolution near CP at $\varrho = 0.05\ mM/s, K_\infty = 7.86\ mM$

Here, we present the transient behavior of the neuronal system near the cusp at $\varrho = 0.05$ mM/s and $K_\infty = 7.86$ mM. As we can see in Figures 18a and 18b, the neuron exhibits episodic bursting behavior. However, the frequency of bursting is notably lower compared to the previously observed case near the generalized Hopf point at $\varrho = 0.025\ mM/s$ and $K_\infty = 13.06\ mM$. This suggests that while the neuron is still in a seizure-like regime, the bursting dynamics are less intense, indicating proximity to the boundary between pathological and physiological states. The plot shows that, under these parameters, the neuron exhibits significantly reduced bursting activity with only one burst within a 100-second interval. The proximity of the cusp point to the stationary region is the primary reason for the observed low neuronal bursting activity. In Figure 18b, the limit cycle exhibits a pronounced elongation in one direction, primarily due to the interaction between the limit point curve and Hopf curves, which is a sign of homoclinic bifurcation.

4.4.4 Time evolution near BT point at $\varrho = 0.82\ mM/s$, $K_\infty = 2.803\ mM$

Here we present the time simulation near the Bogdanov-Takens bifurcation point. As shown, the Bogdanov-Takens bifurcation occurs at a very low value of $K_\infty =$

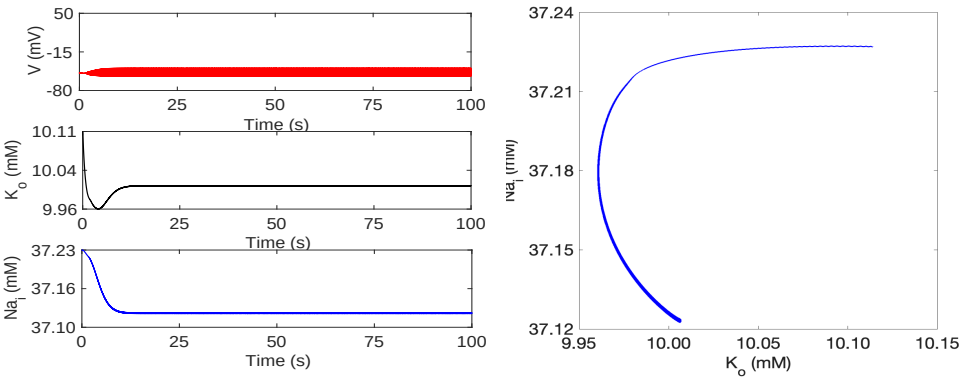

(a) (b)

Fig. 16: Time evolution of neuronal model near generalized Hopf point at $\varrho = 0.06\ mM/s, K_\infty = 13.31\ mM$ in the $\varrho - K_\infty$ parametric plane. Other parameters are set to $\epsilon = 1.33\ s^{-1}, gGlia = 15\ mM/s$. In Figure 16a, the evolution of membrane action potential, $[K^+]_o$ and $[Na^+]_i$ is shown. In Figure 16b, the phase-plane trajectory of $[K^+]_o$ versus $[Na^+]_i$ under the same parameter set is shown, showing convergence to a stationary point, characteristic of the stable steady-state near the generalized Hopf bifurcation.

2.803 mM. At such low extracellular potassium levels, the neuron consistently settles into a stationary state, regardless of the initial conditions. This behavior is observed in Figures 19a and 19b. For $K_\infty \leq 2.803\ mM$, restoring oscillatory activity requires an increase in the pump strength above $\varrho = 0.82\ mM/s$. This highlights the strong influence of ion homeostasis on neuronal excitability and the critical role of the Bogdanov–Takens point in defining the boundary between quiescent and active regimes.

4.5 Bifurcation diagram and stability boundary in $I_{ext} - \varrho$ plane

As already discussed, I_{ext} provides positive feedback to pump strength, which changes the firing pattern of neurons. In this section, the simultaneous effect of I_{ext} and ϱ on the stability of the neuron is studied using codim-2 bifurcation analysis. By scanning the $I_{ext} - \varrho$ plane, we detect two generalized Hopf points and one cusp point, as shown in Figure 20. For lower values of ϱ, the system is in a stationary state, which means there is no neuronal firing. For a positive stimulus current, the neuron starts exhibiting oscillatory behavior. For instance, at $I_{ext} = 3\ \mu A/cm^2$, the neuron exhibits oscillatory $\varrho \geq 0.03\ mM/s$ as well as stationary behavior for $\varrho \leq 0.03\ mM/s$. For a fixed value of ϱ, with an increase in I_{ext}, the neuron first remains at equilibrium.

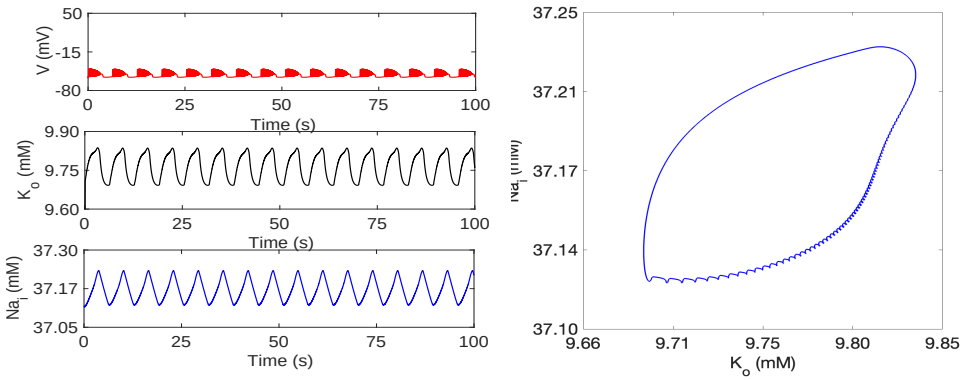

(a) (b)

Fig. 17: Time evolution of the UBC neuronal model near the generalized Hopf bifurcation point, located at $\varrho = 0.025\ mM/s, K_\infty = 13.06\ mM$ in the $\varrho - K_\infty$ plane. The simulation was performed using $\epsilon = 1.33\ s^{-1}, gGlia = 15\ mM/s$. In Figure 17a, the evolution of membrane action potential, $[K^+]_o$ and $[Na^+]_i$ is shown; in Figure 17b, a phase-plane representation of $[K^+]_o$ versus $[Na^+]_i$ under the same parameter conditions is shown, illustrating the emergence of a bursting behavior near the generalized Hopf point.

Bifurcations	$\varrho\ (mM/s)$	$I_{ext}\ \mu A/cm^2$
CP	0.07	1.65
GH	0.03	3.00
GH	0.06	3.18

Table 7: Bifurcation points in $I_{ext} - \varrho$ plane

As I_{ext} is increased, the neuron transitions to oscillatory behavior, and with a further increase in I_{ext}, for higher values, the system enters a depolarization regime.

The neuron exhibits multistability within a narrow parameter region. For a fixed value of I_{ext} between 1.65 and 3.18 $\mu A/cm^2$, the system undergoes two Hopf bifurcations as ϱ varies. At low ϱ, the neuron transitions from a stationary state to an oscillatory state via a Hopf bifurcation. As ϱ increases further, it reverts to a stationary state through a second Hopf bifurcation. This sequence indicates alternating stability and the presence of multistable dynamics. At the cusp point, the two limit points

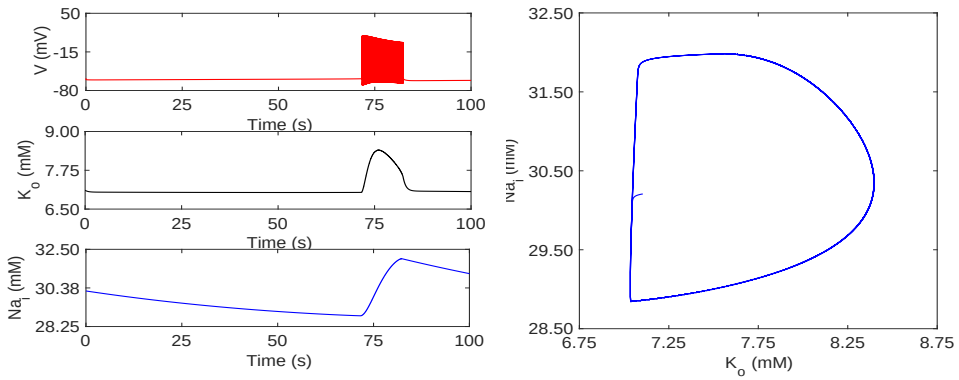

(a) (b)

Fig. 18: Time evolution of the UBC neuronal model near the cusp point bifurcation, located at $\varrho = 0.05\ mM/s, K_\infty = 7.86\ mM$ in the $\varrho - K_\infty$ plane. The simulation was performed using $\epsilon = 1.33\ s^{-1}, gGlia = 15\ mM/s$. In Figure 18a, the evolution of the membrane action potential, $[K^+]_o$ and $[Na^+]_i$, is shown; in Figure 18b, the phase-plane representation of $[K^+]_o$ versus $[Na^+]_i$ under the same parameter conditions is shown, illustrating the emergence of a bursting behavior near the cusp point.

collide and vanish. Therefore, below the cusp point, no limit points remain, implying the absence of multistability and hysteresis in the neuron. A list of the detected bifurcation points and the corresponding parameters is provided in Table 7.

4.5.1 Time evolution near GH point at $\varrho = 0.06\ mM/s$, $I_{ext} = 3.18\ \mu A/cm^2$

In Figures 21a and 21b, the time evolution of the membrane action potential, extracellular potassium ion, and intracellular sodium ion is presented in the proximity of the generalized Hopf point at $\varrho = 0.06\ mM/s, I_{ext} = 3.18\ \mu A/cm^2$. It is observed that the neurons show frequent bursting with low-amplitude subthreshold oscillations. Membrane action potential oscillates in a small band between $V = -70\ mV$ and $V = -30\ mV$ and fails to generate a full action potential. In this scenario, bursting occurs more frequently, although the burst and silent phases are very brief. The bursting frequency matches the frequency of slow variable K_o. The neuron is sustaining oscillations, and the trajectory is forming a small-radius, outlined loop of a limit cycle. We can say the ion concentration practically remains constant

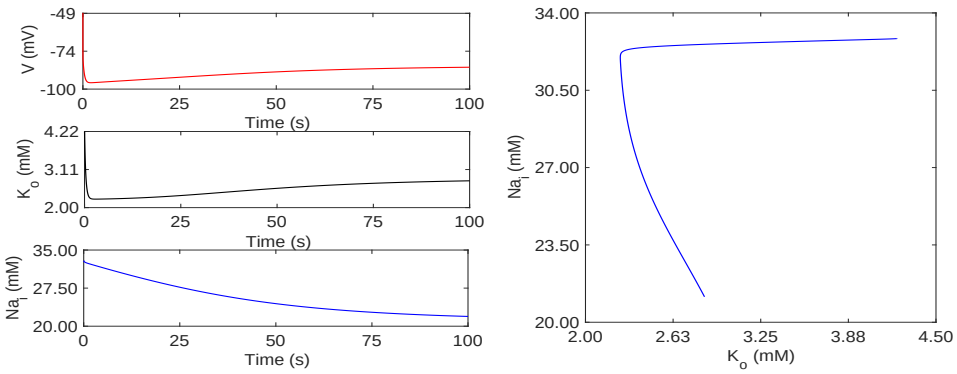

(a) (b)

Fig. 19: Time evolution of the UBC model near the Bogdanov-Takens point, located at $\varrho = 0.82\ mM/s$ and $K_\infty = 2.803\ mM$ in the $K_\infty - \varrho$ parametric plane. Figure 19a shows the time courses of the membrane action potential, $[K^+]_o$, and $[Na^+]_i$. Figure 19b shows the phase-plane trajectory of $[K^+]_o$ versus $[Na^+]_i$ corresponding to the dynamics shown in Figure 19a, illustrating the system's behavior near the Bogdanov-Takens point.

4.5.2 Time evolution near GH point at $\varrho = 0.03\ mM/s$, $I_{ext} = 3\ \mu A/cm^2$

In this section, the neural dynamics are presented in the proximity of the GH point ($\varrho = 0.03\ mM/s, I_{ext} = 3\ \mu A/cm^2$). The dynamics of the membrane action potential, extracellular potassium ion, and intracellular sodium ion are illustrated in Figures 22a and 22b, respectively. It is observed that the neurons show subthreshold small-amplitude bursting, and the membrane action potential oscillates between $V = -65\ mV$ and $V = -30\ mV$. Slow variables K_o and Na_i shows small-amplitude oscillations between $K_o = 5.5\ mM - K_o = 6.25\ mM$ and $Nai = 36.15\ mM - 36.85\ mM$. The change in slow variables matches the bursting frequency. In phase space, the trajectory forms an outlined loop like a stable attractor. The corresponding phase portrait is asymmetric and elongated in one direction, suggesting the influence of a saddle node.

The limit cycle involving potassium and sodium ions has a small radius, indicating that their concentrations remain nearly constant. The neuron operates near a critical point, close to seizure activity, where small disturbances can trigger seizures.

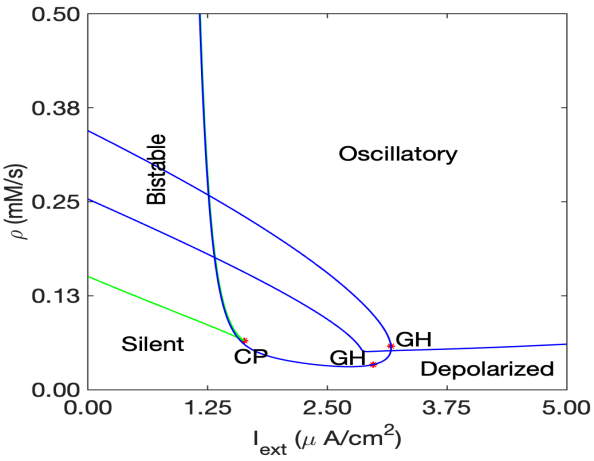

Fig. 20: Codim-2 bifurcation and the stability boundary in $\varrho - I_{\text{ext}}$ space; the region between LP curves is a bistable region; the region between Hopf curves is oscillatory, and outside the Hopf curves, neurons are in equilibrium

4.5.3 Time evolution near CP at $\varrho = 0.07\ mM/s$, $I_{ext} = 1.65\ \mu A/cm^2$

As shown in Figure 20, the cusp point $\varrho = 0.07\ mM/s$, $I_{\text{ext}} = 1.65\ \mu A/cm^2$ lies near the stability boundary in the ϱ–I_{ext} parameter plane. In the proximity of this point, the neuron exhibits bursting behavior, though the bursts occur infrequently and are separated by prolonged silent phases. Figures 23a and 23b reveal that the membrane action potential and potassium ion concentration exhibit large-amplitude oscillations, with rapid transitions between their extrema. Additionally, the associated limit cycle has a broader span than those observed in previous cases. As explained in earlier cases, the rise in $[K^+]_o$ level is an indication of seizure initiation. The limit cycle is prolonged in one direction, which is a sign of interaction between the limit point curve and Hopf curve, and the neuron is entering a homoclinic bifurcation.

5 Conclusion

In this article, we present a quantitative comparison between the reduced Barreto-Cressman (RBC) model and the Barreto-Cressman (BC) model, followed by a detailed codim-1 and codim-2 bifurcation analysis of the unified Barreto-Cressman (UBC) model. Since bath potassium concentration (K_∞), pump strength (ϱ), and

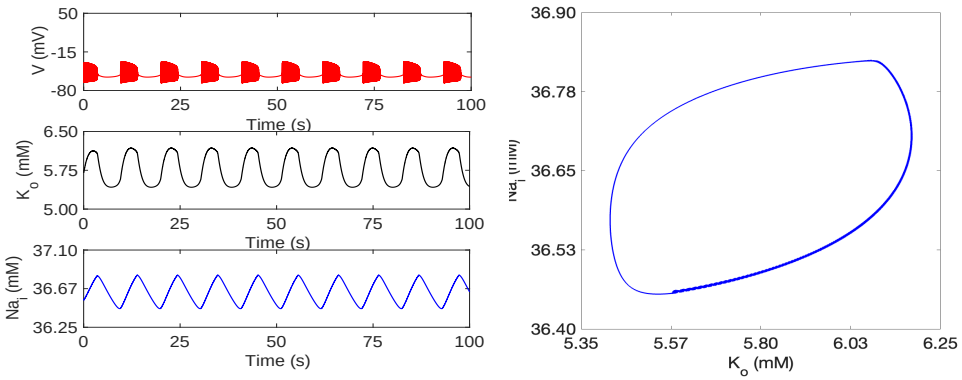

(a) (b)

Fig. 21: Time evolution of the UBC neuronal model near the generalized Hopf bifurcation point, located at $\varrho = 0.06\ mM/s, I_{ext} = 3.18\ \mu A/cm^2$ in the $\varrho - I_{ext}$ plane. The simulation was performed using $K_\infty = 5\ mM, \epsilon = 1.33\ s^{-1}, gGlia = 15\ mM/s$. In Figure 21a, the evolution of the membrane action potential, $[K^+]_o$ and $[Na^+]_i$, is shown; in Figure 21b, the phase-plane representation of $[K^+]_o$ versus $[Na^+]_i$ under the same parameter conditions is shown, illustrating the emergence of bursting near the generalized Hopf point.

external stimulus current (I_{ext}) play a crucial role in neuronal hyperactivity, our focus is on bifurcation analysis concerning K_∞, I_{ext}, and ϱ. The primary objective of this study is to identify key bifurcation points and parameter regions that govern neuronal dynamics, to gain deeper insight into the emergence of bursting behavior and transitions into pathological states like seizures.

The RBC model effectively captures the qualitative dynamics of the BC model at lower values of ϱ and K_∞. A minor phase shift between the RBC and BC models is observed, which can be corrected by appropriately adjusting the external stimulus current. However, at higher values of ϱ and K_∞, a noticeable shift in the bifurcation points is observed between the two models. This discrepancy is likely due to the averaging of fast variables inherent in the RBC formulation. Notably, the BC model reveals two limit points that are not captured in the RBC model, indicating that certain transitions in neuronal dynamics are bypassed in the reduced representation.

In the UBC model, chloride dynamics is incorporated into the original BC framework, and a bifurcation analysis is conducted. The results indicate that the inclusion of chloride dynamics leads to neuronal stabilization when the glia clearance constant is high. To restore oscillatory activity, the glia clearance constant is reduced but kept

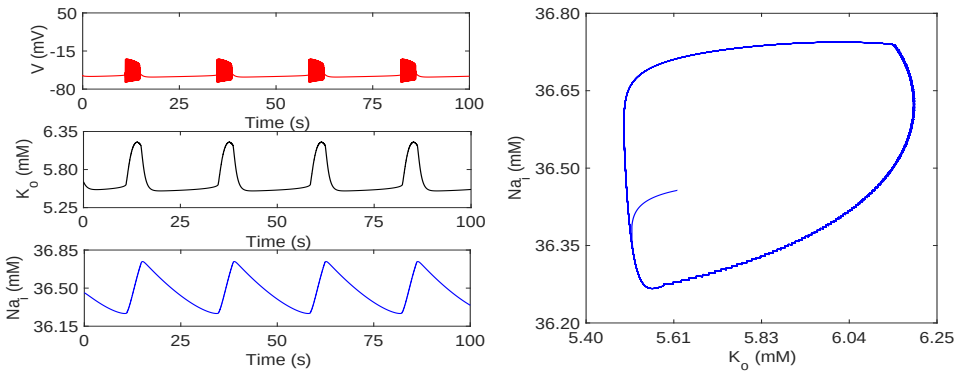

(a) (b)

Fig. 22: Evolution of UBC neuronal model near generalized Hopf point in $I_{ext} - \varrho$ parametric plane. The parameters are set to: $\varrho = 0.03\ mM/s, K_\infty = 5\ mM, \epsilon = 1.33\ s^{-1}, gGlia = 15\ mM/s, I_{ext} = 3\ \mu A/cm^2$. Figure 22a illustrates the temporal evolution of the membrane action potential, $[K^+]_o$, and $[Na^+]_i$. Figure 22b shows the corresponding phase-space trajectory of $[K^+]_o$ vs $[Na^+]_i$, illustrating the emergence of bursting behavior and the nature of the limit cycle near the generalized Hopf point, where the system transitions between supercritical and subcritical Hopf bifurcations.

in the physiological range, and a subsequent bifurcation analysis is performed to investigate the resulting changes in neural dynamics. Codim-2 bifurcation analysis reveals that neurons can exhibit multistability for low values of glia clearance strength and pump strength with K_∞ in the range of 12–13 mM. A similar behavior is observed in the $\varrho - I_{ext}$ plane, where multistability arises for low pump strength with I_{ext} between 1.65 $\mu A/cm^2$ and 3.18 $\mu A/cm^2$. Notably, when the system operates near the SubH bifurcation point, the neuron shows bistable behavior and can alternate between oscillatory and stationary regimes, giving rise to episodic bursting behavior. These findings highlight the critical role of bath potassium concentration, pump strength, and external stimulus current in shaping the overall dynamics of neuronal activity. We can extend this work to study the stability of networks by adding network topology with different mechanisms, such as oxygen dynamics and ATP metabolism, to get a more realistic biophysical model and its stability.

CRediT Authorship Contribution Statement

Niteen Kumar: Conceptualization, Methodology, Discussion, Writing.
Stefano Pagani: Conceptualization, Discussion, Review.

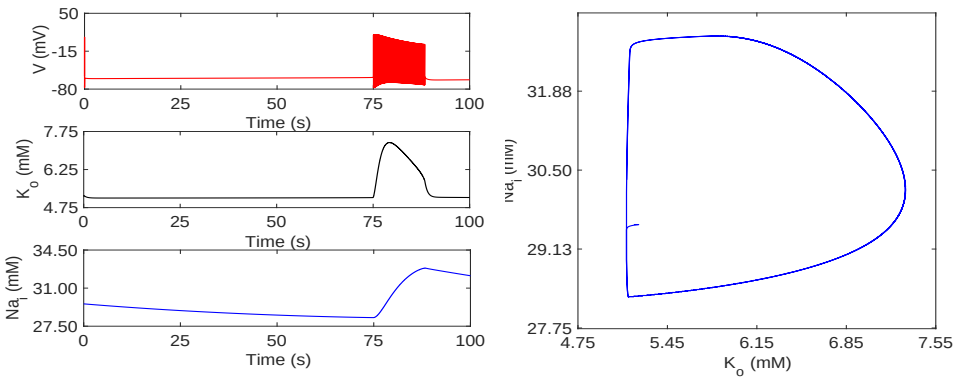

(a) (b)

Fig. 23: Evolution of neuronal dynamics near the cusp point in the $I_{ext} - \varrho$ parametric space; the system parameters are set as follows: ($\varrho = 0.07\ mM/s, K_\infty = 5\ mM, \epsilon = 1.33\ s^{-1}, gGlia = 15\ mM/s, I_{ext} = 1.65\ \mu A/cm^2$). Figure 23a illustrates the temporal evolution of the membrane action potential, $[K^+]_o$ and $[Na^+]_i$. Figure 23b shows the corresponding phase-space trajectory, depicting the evolution of $[K^+]_o$ vs $[Na^+]_i$.

Paola F. Antonietti: Conceptualization, Discussion, Review.
Suneet Singh: Conceptualization, Discussion, Review.

Acknowledgements.

- NK, PFA, SP are members of INdAM-GNCS
- The present research is part of the activities of the Dipartimento di Eccellenza 2023-2027 grant, funded by MUR.
- This work is supported by the Italian Ministry of University and Research (MUR) under the Young Researchers 2024 program, Project SOE2024-0000089 – SACMS: Stability Analysis and Control Mechanisms of Seizures (CUP D43C 24002430001), funded by the European Union – NextGenerationEU through the National Recovery and Resilience Plan (PNRR), Mission 4, Component 2, Investment 1.2, Grant Decree D.D. No. 20 of 21 January 2025.

Declarations

The authors declare that they have no known competing financial interests or personal relationships that could have appeared to influence the work reported in this paper.

- Funding: This work was supported by the Italian Ministry of University and Research (MUR) under the Young Researchers 2024 program, Project SOE2024-0000089 – SACMS: Stability Analysis and Control Mechanisms of Seizures (CUP D43C 24002430001).
- Conflict of interest / Competing interests: The authors have no relevant financial or non-financial interests to disclose.
- Ethics approval and consent to participate: Not applicable.
- Consent for publication: Not applicable.
- Data availability: The datasets generated and/or analyzed during the current study are available from the corresponding author upon reasonable request.
- Materials availability: Materials are available from the corresponding author upon reasonable request.
- Code availability: The code generated during the current study is available from the corresponding author upon reasonable request.
- Author contribution: All authors contributed to the study conception and design. Methodology development and analysis were performed by Niteen Kumar. The first draft of the manuscript was written by Niteen Kumar, and all authors contributed to reviewing the manuscript. All authors read and approved the final manuscript.

References

[1] Meunier, C.: Biological Cybemetics Two and three dimensional reductions of the Hodgkin-Huxley system: separation of time scales and bifurcation schemes (1992)

[2] J. R. Cressman, J.Z.S.J.S.E.B. G. Ullah: The influence of sodium and potassium dynamics on excitability, seizures, and the stability of persistent states: I. single neuron dynamics. Journal Computational Neuroscience **26**(2), 159–170 (2009)

[3] E. Barreto, J.R.C.: Ion concentration dynamics as a mechanism for neuronal bursting. Journal of biological physics **37**, 361–373 (2011) https://doi.org/10.1007/s10867-010-9212-6

[4] J. Ziburkus, E.B. J. R. Cressman, Schiff, S.J.: Interneuron and pyramidal cell interplay during in vitro seizure-like events. Journal of Neurophysiology **95**, 3948–3954 (2006) https://doi.org/10.1152/jn.01378.2005

[5] R. F. Galán, N.N.U. G. B. Ermentrout: Optimal time scale for spike-time reliability: Theory, simulations, and experiments. Journal of Neurophysiology **99**, 277–283 (2008) https://doi.org/10.1152/jn.00563.2007

[6] J. E. Rubin, D.T.: High frequency stimulation of the subthalamic nucleus eliminates pathological thalamic rhythmicity in a computational model. Journal Computational Neuroscience **16**, 211–235 (2004)

[7] Rinzel, J.: Excitation Dynamics: Insights from Simplified Membrane Models. In: Federation Proceedings (1985)

[8] Berger, H.: Uber das elektrenkephalogramm des menschen. Archiv fur Psychiatrie und nervenkrankheiten **98**, 231–254 (1933) https://doi.org/10.1007/BF01814645

[9] A.L. Hodgkin, A.F.H.: A quantitative description of membrane current and its application to conduction and excitation in nerve. Journal of physioligy **117(500-544)** (1952)

[10] C. Morris, H.L.: Voltage oscillations in the barnacle giant muscle fiber. Journal of Biophysics **35**, 193–213 (1981)

[11] FitzHugh, R.: Impulses and physiological states in theoretical models of nerve membrane. Journal of Biophysics **1**, 445–466 (1961)

[12] F. Amzica, A.M. M. Massimini: A spatial buffering during slow and paroxysmal sleep oscillations in cortical networks of glial cells in vivo. Journal of Neuroscience **22**, 1042–1053 (2002)

[13] U. Heinemann, M.J.G. H. D. Lux: Extracellular free calcium and potassium during paroxysmal activity in the cerebral cortex of the cat. Experimental Brain Research **27**, 237–243 (1977) https://doi.org/10.1007/BF00235500

[14] W. J. Moody, A.D.P. K. J. Futamachi: Extracellular potassium activity during epileptogenesis. Experimental Neurology **42**, 248–263 (1974) https://doi.org/10.1016/0014-4886(74)90023-5

[15] C. B. Ransom, H.S. B. R. Ransom: Activity-dependent extracellular k+ accumulation in rat optic nerve: the role of glial and axonal na+ pumps. The Journal of Physiology **522**, 427–442 (2000) https://doi.org/10.1111/j.1469-7793.2000.00427.x

[16] H. Kager, G.G.S. W. J. Wadman: Simulated seizures and spreading depression in a neuron model incorporating interstitial space and ion concentrations. J Neurophysiol **84**, 495–512 (2000)

[17] Yina Wei, S.J.S. Ghanim Ullah: Unification of neuronal spikes, seizures, and spreading depression. Neurobiology of disease, the journal of neuroscience **35**, 11733–11743 (2014)

[18] Strogatz, S.H.: Nonlinear Dynamics and Chaos with Application to Physics, Biology, Chemistry, and Engineering. CRC Press Taylor Francis Group, ??? (2015)

[19] E. M. Izhikevich, E.C.W.F.C.H. N. S. Desai: Bursts as a unit of neural information: selective communication via resonance. Trends Neurosci **26**, 161–167 (2003)

[20] Izhikevich, E.M.: Simple model of spiking neurons. IEEE Trans Neural Networks

14, 1569–1572 (2003)

[21] J. L. Hindmarsh, R.M.R.: A model of neuronal bursting using three coupled first-order differential equations. Proc R Soc Lond B **221**, 87–102 (1984)

[22] J. Nagumo, S.Y. S. Arimoto: An active pulse transmission line simulating nerve axon. Proc IRE **50**, 2061–2070 (1962)

[23] Wu, X.X.: Effects of extracellular potassium diffusion on electrically coupled neuron networks. Physical Review E **022712**, 1–10 (2015)

[24] X. X. Wu, J.W.S.: Multistability in a neuron model with extracellular potassium dynamics. Physical Review E **85** (2012)

[25] M. Bazhenov, M.S. I. Timofeev: Potassium model for slow (2–3 hz) in vivo neocortical paroxysmal oscillations. Journal of NeuroPhysiology **92** (2004)

[26] A. H. Erhardt, J.E.S. K. A. Mardal: Dynamics of a neuron-glia system: the occurrence of seizures and the influence of electroconvulsive stimuli a mathematical and numerical study. Journal Computational Neuroscience **48**, 229–251 (2020)

[27] A. Dhooge, Y.A.K. W. Govaerts: Matcont: A matlab package for numerical bifurcation analysis of odes. ACM Transactions on Mathematical Software (TOMS) **29**, 141–164 (2003) https://doi.org/10.1145/779359.779362

[28] K. D. Rienecker, R.N.S. R. G. Poston: Merits and limitations of studying neuronal depolarization dependent processes using elevated external potassium. American Society for neurochemistry **12**, 1–17 (2020)

[29] N. Hubel, G.U. R. D. Andrew: Large extracellular space leads to neuronal susceptibility to ischemic injury in a na+/k+ pump–dependent manner. Journal of Computational Neuroscience **40**, 177–192 (2016) https://doi.org/10.1007/s10827-016-0591-y

[30] D. Attwell, S.B.L.: An energy budget for signaling in the grey matter of the brain. Journal of Cerebral Blood Flow Metabolism **21(10)**, 1133–1145 (2001)

[31] F. A. Henn, A.H.: Glial cell function: Uptake of transmitter substances. Proceedings of the National Academy of Sciences **68**(11), 2686–2690 (1971)

MOX Technical Reports, last issues

Dipartimento di Matematica
Politecnico di Milano, Via Bonardi 9 - 20133 Milano (Italy)

83/2026 Cavazzutti, M.; Palummo, A.; Arnone, E.; Sun, Y.; Genton, M.G.; Sangalli, L.M.
Voronoi Depth for functional data over non-convex multidimensional supports

82/2026 Botteghi, N.; Tomasetto, M.; Manzoni, A.
Reinforcement learning for control of partial differential equations

81/2026 Clemente, A.; Palummo, A.; Arnone, E.; Aston, J.A.D.; Panzica, F.; Sangalli, L.M.
Modeling spatio-temporal smoothness using nonlinear differential operators

80/2026 Botteghi, N; Glas, S; Brune, C
Deep Invertible Autoencoders for Dimensionality Reduction of Dynamical Systems

78/2026 Botteghi, N; Brook, O; Fasel, U; Califano, F
Interconnection and Damping Assignment Passivity-Based Control using Sparse Neural ODEs

79/2026 Vitullo, P.; Macaluso, C.; Gazzoni, S.; Cassanmagnago, A.; Dimola, N.; Possenti, L.; Zunino, P.
A computational model for phenotype-structured tumour dynamics with reduced microvascular oxygen and event-based radiotherapy

77/2026 Renzi, F.; Pagani, S.; Antonietti, P.F.; Vergara, C.
A Neural-Network Approach for the Stability of Loosely-Coupled FSI Simulations in Hemodynamics

75/2026 Botteghi, N; Tomasetto, M; Fasel, U; Braghin, F; Manzoni, A
HypeMARL: Multi-Agent Reinforcement Learning For High-Dimensional, Parametric, and Distributed Systems

76/2026 Pizzamiglio, S.M.; Pagani, S.; Regazzoni, F.
Learning PDE solution operators with variable initial conditions via Latent Dynamics Networks

74/2026 Brivio, S.; Franco, N. R.
Deep Symmetric Autoencoders from the Eckart-Young-Schmidt Perspective